ESC-TR-94-085

Quarterly Technical Report

Solid State Research

1994:1

Lincoln Laboratory

MASSACHUSETTS INSTITUTE OF TECHNOLOGY

LEXINGTON, MASSACHUSETTS

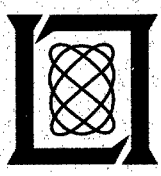

Prepared for the Department of the Air Force under Contract F19628-90-C-0002.

This report is based on studies performed at Lincoln Laboratory, a center for research operated by Massachusetts Institute of Technology. The work was sponsored by the Department of the Air Force under Contract F19628-90-C-0002.

The ESC Public Affairs Office has reviewed this report, and it is releasable to the National Technical Information Service, where it will be available to the general public, including foreign nationals.

This technical report has been reviewed and is approved for publication.

FOR THE COMMANDER

Gary Tatungian
Administrative Contracting Officer
Contracted Support Management

MASSACHUSETTS INSTITUTE OF TECHNOLOGY
LINCOLN LABORATORY

SOLID STATE RESEARCH

QUARTERLY TECHNICAL REPORT

1 NOVEMBER 1993 — 31 JANUARY 1994

ISSUED 27 JULY 1994

LEXINGTON MASSACHUSETTS

ABSTRACT

This report covers in detail the research work of the Solid State Division at Lincoln Laboratory for the period 1 November 1993 through 31 January 1994. The topics covered are Electrooptical Devices, Quantum Electronics, Materials Research, Submicrometer Technology, High Speed Electronics, Microelectronics, and Analog Device Technology. Funding is provided primarily by the Air Force, with additional support provided by the Army, ARPA, Navy, BMDO, NASA, and NIST.

TABLE OF CONTENTS

LIST OF ILLUSTRATIONS

LIST OF ILLUSTRATIONS (Continued)

LIST OF ILLUSTRATIONS (Continued)

LIST OF TABLES

INTRODUCTION

1. ELECTROOPTICAL DEVICES

Single- and multiple-quantum-well strained-layer InGaAsP/InP structures for diode laser operation at 1.3-μm wavelength have been grown by atmospheric-pressure organometallic vapor phase epitaxy. Threshold current densities and differential efficiencies of broad-area devices are among the best reported for InGaAsP/InP lasers at this wavelength.

Parallel free-space optical interconnection modules have been designed, fabricated, and assembled with monolithic arrays of 980-nm ridge-waveguide diode lasers, photoformed-glass microlenses, InGaAs/InP photodiodes, and GaAs heterojunction bipolar receivers. The overall system has 20–80% transition times of 100 ps (rise) and 120 ps (fall) and low cross talk between optical data paths.

2. QUANTUM ELECTRONICS

A Ho:YAG laser end-pumped by 1.9-μm diode lasers has generated 0.67-W CW output power at an operating temperature of –53°C. The laser has been operated at heatsink temperatures as high as 60°C.

3. MATERIALS RESEARCH

Double-heterostructure GaInAsSb/AlGaAsSb diode lasers emitting at 3 μm have exhibited pulsed operation at temperatures up to 255 K and CW operation up to 170 K, with CW output power of 45 mW/facet at 100 K. The lowest pulsed threshold current density is 9 A/cm^2 obtained at 40 K.

4. SUBMICROMETER TECHNOLOGY

Photoresist reflow techniques have been developed for the fabrication of high-quality microlenses. Preshaping the photoresist structures prior to reflow minimizes the spherical aberrations in high-f-number lenses.

A new spin-on antireflective layer composed of a polymeric dye and transparent base polymer has been developed for 193-nm lithography. The layer reduces thin-film interference effects in single-layer photoresists, which can seriously degrade the patterning performance of optical lithography systems.

5. HIGH SPEED ELECTRONICS

A photomixer based on low-temperature-grown (LTG) GaAs has demonstrated an output power that is flat to ~ 250 GHz and a high optical-to-electrical conversion efficiency, with the highest frequency measured to date being 3.8 THz. Relative to other photoconductors of comparable frequency response, LTG GaAs has very low photocarrier recombination time (< 1 ps), high dc breakdown field (> 10^6 V cm^{-1}), and high photocarrier mobility (~ 200 cm^2 V^{-1} s^{-1}).

6. MICROELECTRONICS

A two-dimensional charge-coupled device (CCD) array capable of transferring charge packets in all four directions has been demonstrated in a 64 × 64 prototype device. Applications include astronomical imaging where the charge shifting can be made to track the tip-tilt correction for atmospheric turbulence and thereby improve image resolution.

The sensitivity of CCD arrays for detection of ^{32}P beta particles, a common radioisotope label used in DNA sequencing, has been evaluated. Experimental measurements showed the CCD detector has near ideal detection performance for this particular beta particle, and in a preliminary experiment using the ^{32}P label the CCD detector successfully identified DNA sequences by the method of sequencing by hybridization.

7. ANALOG DEVICE TECHNOLOGY

A single-chip CCD/CMOS multibit far-infrared filter has been designed. In this device a novel bit-serial, pipelined CCD multiplying digital-to-analog converter is used to achieve low power consumption.

REPORTS ON SOLID STATE RESEARCH

1 NOVEMBER 1993 THROUGH 31 JANUARY 1994

PUBLICATIONS

New Single-Layer Positive Resists for 193- and 248-nm Lithography Using Methacrylate Polymers	R. D. Allen* G. M. Wallraff* W. D. Hinsberg* W. E. Conley* R. R. Kunz	*Solid State Technol.* **36** (11), 53 (1993)
Monolithic Optoelectronic Transistor: A New Smart-Pixel Device	B. F. Aull K. B. Nichols P. A. Maki S. C. Palmateer E. R. Brown T. A. Lind	*Appl. Phys. Lett.* **63**, 1555 (1993)
Resonant Tunneling Through Mixed Quasibound States in a Triple-Well Structure	E. R. Brown C. D. Parker A. R. Calawa M. J. Manfra	*Appl. Phys. Lett.* **62**, 3016 (1993)
A Quasioptically Stabilized Resonant-Tunneling-Diode Oscillator for the Millimeter- and Submillimeter-Wave Regions	E. R. Brown C. D. Parker K. M. Molvar K. D. Stephan*	*IEEE Trans. Microwave Theory Tech.* **40**, 846 (1992)
Single-Frequency GaInAsSb/AlGaAsSb Quantum-Well Ridge-Waveguide Lasers Emitting at 2.1 μm	H. K. Choi S. J. Eglash M. K. Connors	*Appl. Phys. Lett.* **63**, 3271 (1993)
GaInAsSb-AlGaAsSb Tapered Lasers Emitting at 2 μm	H. K. Choi J. N. Walpole G. W. Turner S. J. Eglash L. J. Missaggia M. K. Connors	*IEEE Photon. Technol. Lett.* **5**, 1117 (1993)

*Author not at Lincoln Laboratory.

CW Operation of Monolithic Arrays of Surface-Emitting AlGaAs Diode Lasers with Dry-Etched Vertical Facets and Parabolic Deflecting Mirrors	J. P. Donnelly W. D. Goodhue C. A. Wang R. J. Bailey G. A. Lincoln G. D. Johnson L. J. Missaggia J. N. Walpole	*IEEE Photon. Technol. Lett.* **5**, 1146 (1993)
New Photoresist Processes at UV Wavelengths Less Than 200 Nanometers	D. J. Ehrlich R. R. Kunz M. A. Hartney M. W. Horn J. Melngailis	In *Irradiation of Polymeric Materials: Processes, Mechanisms, and Applications,* E. Reichmanis, C. W. Frank, and J. H. O'Donnell, eds. (American Chemical Society, Washington, D.C., 1993), Chap. 17
Lasers, Solid-State	T. Y. Fan	In *Encyclopedia of Applied Physics,* Vol. 8 (VCH Publishers, New York, 1994), pp. 443-463
Controlled *p*-Type Sb Doping in LPE-Grown $Hg_{1-x}Cd_xTe$ Epilayers	T. C. Harman	*J. Electron. Mater.* **22**, 1165 (1993)
Use of Quantum-Well Superlattices to Obtain a High Figure of Merit from Nonconventional Thermoelectric Materials	L. D. Hicks* T. C. Harman M. S. Dresselhaus*	*Appl. Phys. Lett.* **63**, 3230 (1993)
Laser Physics	P. L. Kelley* J. J. Zayhowski	In *Encyclopedia of Applied Physics,* Vol. 8 (VCH Publishers, New York, 1994), pp. 299-320
Resist Alternatives for Sub-0.35-μm Lithography by Using Highly Attenuated Radiation	R. R. Kunz M. A. Hartney M. Rothschild	*Appl. Opt.* **32**, 7032 (1993)

*Author not at Lincoln Laboratory.

*Author not at Lincoln Laboratory.

Comparison of the Surface Morphology and Microstructure of In Situ and Ex Situ Derived $YBa_2Cu_3O_{7-x}$ Thin Films	A. C. Westerheim P. C. McIntrye* S. N. Basu* D. Bhatt* L. S. Yu-Jahnes A. C. Anderson M. J. Cima*	*J. Electron. Mater.* **22**, 1113 (1993)
Diode-Pumped Composite-Cavity Electrooptically Tuned Microchip Laser	J. J. Zayhowski P. A. Schulz C. Dill III S. R. Henion	*IEEE Photon. Technol. Lett.* **5**, 1153 (1993)

ACCEPTED FOR PUBLICATION

A New Face-Centered-Cubic Photonic Crystal for Microwave and Millimeter-Wave Applications	E. R. Brown C. D. Dill C. D. Parker K. Agi* K. J. Malloy*	*Appl. Phys. Lett.*
Double-Heterostructure Diode Lasers Emitting at 3 μm with a Metastable GaInAsSb Active Layer and AlGaAsSb Cladding Layers	H. K. Choi S. J. Eglash G. W. Turner	*Appl. Phys. Lett.*
High-Power GaInAsSb-AlGaAsSb Multiple-Quantum-Well Diode Lasers Emitting at 1.9 μm	H. K. Choi G. W. Turner S. J. Eglash	*IEEE Photon. Technol. Lett.*
InAsSb/AlAsSb Double-Heterostructure Diode Lasers Emitting at 4 μm	S. J. Eglash H. K. Choi	*Appl. Phys. Lett.*
Mosaic Diamond Substrates Approaching Single-Crystal Quality Using Cube-Shaped Diamond Seeds	M. W. Geis N. N. Efremow R. Susalka J. C. Twichell K. A. Snail* C. Spiro* B. Sweeting*	*Int. J. Sci. Technol. Diamond Related Mater.*

*Author not at Lincoln Laboratory.

Applications of Lasers in Microelectronics and Micromechanics	R. R. Kunz M. W. Horn T. M. Bloomstein D. J. Ehrlich	*Appl. Surf. Sci.*
Large-Numerical-Aperture Microlens Fabrication by One-Step Etching and Mass-Transport Smoothing	Z. L. Liau D. E. Mull C. L. Dennis R. G. Waarts*	*Appl. Phys. Lett.*
Tolerances in Microlens Fabrication by Multilevel Etching and Mass-Transport Smoothing	Z. L. Liau D. W. Nam* R. G. Waarts*	*Appl. Phys. Lett.*
Effects of Phase Errors on Coherent Emitter Arrays	C. D. Nabors	*Appl. Opt.*

PRESENTATIONS†

CCD Neural Net VME Board for Pattern Recognition	A. M. Chiang J. R. LaFranchise M. L. Chuang	1993 Government Microcircuit Applications Conference, New Orleans, Louisiana, 1-4 November 1993
Superconductive Electronics	R. W. Ralston	
Superconducting Circuits for a 2-Gigachip-per-Second Spread-Spectrum Modem	J. P. Sage R. W. Ralston	
Advanced Devices Fabricated with Chlorine Ion-Beam-Assisted Etching	W. D. Goodhue	Lincoln Laboratory Technical Seminar Series, Colorado State University, Fort Collins, Colorado, 7 November 1993
Prototyping to Manufacturing: Applications of Lasers in Microelectronics and Micromechanics	D. J. Ehrlich	1st International Symposium on Lasers and Optoelectronics: Techniques and Applications, Singapore, 11-14 November 1993

*Author not at Lincoln Laboratory.

†Titles of presentations are listed for information only. No copies are available for distribution.

Resist Processes for ArF Excimer Laser Lithography	M. W. Horn R. R. Kunz C. L. Keast	40th National American Vacuum Society Symposium, Orlando, Florida, 15-19 November 1993
Progress in Mid-Infrared Diode Lasers	H. K. Choi G. W. Turner J. N. Walpole	IEEE Lasers and Electro-Optics Society Annual Meeting, San Jose, California, 15-18 November 1993
Fabrication of Large-Numerical-Aperture Anamorphic Microlenses and Collimation of Tapered Unstable-Resonator Laser Output	Z. L. Liau J. N. Walpole D. E. Mull C. L. Dennis L. J. Missaggia	
Optoelectronic VLSI Circuit Fabrication	K. V. Shenoy* P. R. Nuytkens* C. G. Fonstad, Jr.* G. D. Johnson W. D. Goodhue J. P. Donnelly	
Tapered Semiconductor Optical Power Amplifiers and Oscillators	J. N. Walpole	
Picosecond Q-Switched Microchip Lasers	J. J. Zayhowski	
Nonlinear Surface Impedance for YBCO Thin Films at High RF Power	P. P. Nguyen D. E. Oates G. Dresselhaus* M. S. Dresselhaus*	1993 Fall Meeting of the Materials Research Society, Boston, Massachusetts, 29 November–3 December 1993
Frequency Dependence of the Surface Impedance in a YBaCuO Thin Film in dc Magnetic Field	S. Revenaz D. E. Oates G. Dresselhaus* M. S. Dresselhaus*	

*Author not at Lincoln Laboratory.

MWIR HgCdTe Lasers	H. Q. Le	Technical Seminar, Rockwell International Science Center, Thousand Oaks, California, 30 November 1993
Photonic-Crystal Planar Antennas for Millimeter Wavelengths	E. R. Brown C. D. Parker J. P. Mattia M. W. Horn	1993 International Semiconductor Device Research Symposium, Charlottesville, Virginia, 1-3 December 1993
Resonant-Tunneling Transmission Lines	C. L. Dennis E. R. Brown S. Prasad*	
Resonant-Tunneling-Diode Circuits	T. C. L. G. Sollner E. R. Brown C. L. Chen C. G. Fonstad* W. D. Goodhue R. H. Mathews J. P. Sage	
Superconducting Cueing Receiver for Space Applications	T. C. L. G. Sollner W. G. Lyons D. R. Arsenault M. M. Seaver R. R. Boisvert B. J. Reynolds	
Diamond Transistor Performance and Fabrication	M. W. Geis J. C. Twichell	Meeting of the New England Chapter, American Vacuum Society, Burlington, Massachusetts, 8 December 1993

*Author not at Lincoln Laboratory.

Mosaic Diamond Substrates Approaching Single-Crystal Quality Using Cube-Shaped Diamond Seeds	M. W. Geis N. N. Efremow R. Susalka J. C. Twichell K. A. Snail* C. Spiro* B. Sweeting* S. Holly*	Materials for High-Temperature Semiconductor Devices, Washington, D.C., 14-15 December 1993
Diamond Review	M. W. Geis J. C. Twichell	
Diamond Field-Emission Cathodes	M. W. Geis J. C. Twichell C. O. Bozler D. D. Rathman N. N. Efremow R. S. Uttaro K. E. Krohn M. Kordesch* M. A. Hollis T. M. Lyszczarz	
Hybrid Electronics for Neural Network System Applications	A. M. Chiang	1993 International Symposium on Artificial Neural Networks, Taipei, Taiwan, 20-23 December 1993
Diode-Pumped Source of Sodium-Resonance Radiation	T. H. Jeys V. Daneu	24th Winter Colloquium on Quantum Electronics, Snowbird, Utah, 6 January 1994
Tapered Semiconductor Optical Power Amplifiers and Oscillators	J. N. Walpole E. S. Kintzer S. R. Chinn C. A. Wang L. J. Missaggia	

*Author not at Lincoln Laboratory.

High-T_c Superconducting Microwave Devices: Some Fundamental Issues in Materials, Physics, and Engineering	N. Newman* W. G. Lyons	International Conference on Millimeter and Submillimeter Waves and Applications, San Diego, California, 10-14 January 1994
Organometallic Vapor Phase Epitaxy for Quantum-Well Diode Lasers	C. A. Wang	Raytheon Research Division Seminar Series, Lexington, Massachusetts, 12 January 1994
Passive Modulators for Antenna Remoting Applications	G. E. Betts C. H. Cox III F. J. O'Donnell K. G. Ray A. C. Yee	4th Annual Symposium on Photonics Systems for Antenna Applications, Monterey, California, 18-22 January 1994
Material Properties and Microwave Applications of HTSC Films	A. C. Anderson	OE/LASE 1994: High-T_c Microwave Superconductors and Applications, Los Angeles, California, 22-28 January 1994
Issues and Applications for Wideband Real-Time Spectral Analysis Systems	W. G. Lyons A. C. Anderson D. R. Arsenault M. M. Seaver R. R. Boisvert T. C. L. G. Sollner	
Optical-Heterodyne Generation in Low-Temperature-Grown GaAs up to 1.2 THz	E. R. Brown K. A. McIntosh F. W. Smith K. B. Nichols M. J. Manfra C. L. Dennis	SPIE Conference on Nonlinear Optics for High-Speed Electronics, Los Angeles, California, 25 January 1994
Diamond Field Emitters for Flat-Panel Displays	J. C. Twichell M. W. Geis T. M. Lyszczarz	High Definition Systems Information Exchange Conference, Arlington, Virginia, 30 January–2 February 1994

Comparison of Oil Thickness Measured Using a Frequency Scanning Radiometer Versus Theoretical Predictions	E. R. Brown G. M. Daniels T. J. Murphy O. B. McMahon G. G. Hogan	2nd Thematic Conference on Remote Sensing for Marine and Coastal Environments, New Orleans, Louisiana, 31 January–2 February 1994

ORGANIZATION

SOLID STATE DIVISION

A. L. McWhorter, *Head*
I. Melngailis, *Associate Head*
E. Stern, *Associate Head*
D. C. Shaver, *Assistant Head*
J. F. Goodwin, *Assistant*

D. J. Ehrlich, *Senior Staff*
N. L. DeMeo, Jr., *Associate Staff*
J. W. Caunt, *Assistant Staff*
K. J. Challberg, *Administrative Staff*

SUBMICROMETER TECHNOLOGY

M. Rothschild, *Leader*
T. M. Lyszczarz, *Assistant Leader*
L. H. Dubois, *Senior Staff*

Astolfi, D. K.
Craig, D. M.
Dennis, C. L.
DiNatale, W. F.
Doran, S. P.
Efremow, N. N., Jr.
Forte, A. R.
Geis, M. W.
Goodman, R. B.
Hartney, M. A.
Horn, M. W.
Keast, C. L.
Kunz, R. R.
Maki, P. A.
Palmateer, S. C.
Sedlacek, J. H. C.
Stern, M. B.
Twichell, J. C.
Uttaro, R. S.

QUANTUM ELECTRONICS

A. Sanchez-Rubio, *Leader*
T. Y. Fan, *Assistant Leader*

Aggarwal, R. L.
Cook, C. C.
Daneu, V.
DeFeo, W. E.
DiCecca, S.
Dill, C. D., III
Hotaling, T. C.
Hsu, L.*
Jeys, T. H.
Kelley, P. L.‡
Le, H. Q.
Ochoa, J. R.
Zayhowski, J. J.

ELECTRONIC MATERIALS

B-Y. Tsaur, *Leader*
D. L. Spears, *Assistant Leader*

Chen, C. K.
Choi, H. K.
Connors, M. K.
Fahey, R. E.
Finn, M. C.
Golovchenko, P. A.
Harman, T. C.
Iseler, G. W.
Krohn, L., Jr.
McGilvary, W. L.
Nitishin, P. M.
Pantano, J. V.
Paul, S. A.*
Reinold, J. H., Jr.
Turner, G. W.
Wang, C. A.

HIGH SPEED ELECTRONICS

R. A. Murphy, *Leader*
M. A. Hollis, *Assistant Leader*

Bozler, C. O.
Brown, E. R.
Chen, C. L.
Goodhue, W. D.
Harris, C. T.
Lincoln, G. A., Jr
Mahoney, L. J.
Manfra, M. J.
Mathews, R. H.
Mattia, J. P.*
McIntosh, K. A.
McMahon, O. B.
Nichols, K. B.
Rabe, S.
Rathman, D. D.

---

* Research Assistant
‡ Leave of Absence

ELECTROOPTICAL DEVICES

R. C. Williamson, *Leader*
L. M. Johnson, *Assistant Leader*

Aull, B. F.
Bailey, R. J.
Betts, G. E.
Donnelly, J. P.
Groves, S. H.
Hovey, D. L.
Liau, Z. L.
Lind, T. A.
Missaggia, L. J.
Mull, D. E.
O'Donnell, F. J.
Palmacci, S. T.
Reeder, R. E.
Roussell, H. V.
Tsang, D. Z.
Walpole, J. N.
Woodhouse, J. D.

ANALOG DEVICE TECHNOLOGY

R. W. Ralston, *Leader*
T. C. L. G. Sollner, *Assistant Leader*
P. M. Mankiewich, *Assistant Leader*
A. C. Anderson, *Senior Staff*
A. M. Chiang, *Senior Staff*

Abusch, D. M.*
Arsenault, D. R.
Boisvert, R. R.
Brogan, W. T.
Denneno, J. M.
Fitch, G. L.
Green, J. B.‡
Holtham, J. H.
LaFranchise, J. R.
Lyons, W. G.
Macedo, E. M., Jr.
Murphy, P. G.
Oates, D. E.
Sage, J. P.
Seaver, M. M.
Slattery, R. L.
Tam, K.*

MICROELECTRONICS

E. D. Savoye, *Leader*
B. B. Kosicki, *Assistant Leader*
B. E. Burke, *Senior Staff*

Clark, H. R., Jr.
Daniels, P. J.
Doherty, C. L., Jr.
Dolat, V. S.
Donahue, T. C.
Felton, B. J.
Gregory, J. A.
Johnson, K. F.
Loomis, A. H.
McGonagle, W. H.
Mountain, R. W.
Percival, K. A.
Reich, R. K.
Thomas, J. W.*
Young, D. J.

* Research Assistant
‡ Leave of Absence

1. ELECTROOPTICAL DEVICES

1.1 1.3-μm STRAINED-LAYER InGaAsP/InP QUANTUM-WELL LASERS WITH LOW THRESHOLD CURRENT DENSITY

InGaAsP/InP epitaxial growth and device processing techniques are being developed for the fabrication of guided-wave optical circuits that utilize integrated optical amplifiers operating at a wavelength of 1.3 μm. Amplifier design requires estimates of transparency current and modal gain, which can be obtained from the characterization of broad-area diode lasers operating at this wavelength. Laser diode performance is also a good indication of the quality of the epitaxial growth techniques. Here, we report laser diode results on some of our initial strained-layer InGaAsP quantum-well laser material. The threshold current densities obtained (as low as 210 A/cm^2) are among the best reported for InGaAsP lasers operating at λ = 1.3 μm.

The diode laser material evaluated had either one or three strained-layer $In_{0.9}Ga_{0.1}As_{0.5}P_{0.5}$ quantum wells centered in a separate-confinement heterostructure (SCH) large optical cavity. The ~ 1% biaxial compression in these wells is comparable to that of InGaAs/GaAs quantum wells operating at 0.98 μm. Unintentionally doped lattice-matched InGaAsP ($\lambda_g \approx 1.04$ μm) was used for both the confinement and barrier layers. The quantum wells and barrier layers were both ~ 10 nm thick. The total thickness of the guiding region, including confining layers, quantum wells and barriers, was ~ 0.5 μm on all devices. The bottom and top cladding layers were n- and p-type InP, respectively, while p^+-$In_{0.53}Ga_{0.47}As$ was used as a top contacting layer.

These structures were grown on n^+-InP substrates by organometallic vapor phase epitaxy (OMVPE) in an atmospheric pressure chimney-geometry reactor incorporating susceptor rotation [1]. Trimethylindium, trimethylgallium, arsine, and phosphine were used as source materials for the alloy constituents, and silane in hydrogen and diethylzinc were used for the n and p doping, respectively. A growth temperature of 650°C was used for all layers except the top p^+-$In_{0.53}Ga_{0.47}As$ contacting layer, which was grown at 600°C to increase the zinc incorporation. The InP substrates had an n-type carrier concentration in the mid-10^{18}-cm^{-3} range and were oriented on-axis in the (100) direction. A typical growth sequence was begun by growing a 1.0-μm-thick n-type InP bottom cladding layer on the n^+ substrate. The doping in this layer was graded from ~ 1×10^{18} to 7×10^{17} cm^{-3}. This was followed by the growth of the lower confining layer, the quantum wells and barrier layers, the upper confining layer, and a 1.5-μm-thick Zn-doped InP top cladding layer. The Zn doping in the top cladding layer was graded from $p = 2.5 \times 10^{17}$ to 5×10^{17} cm^{-3}. A top 0.2-μm-thick p^+-$In_{0.53}Ga_{0.47}As$ layer was then grown at 600°C to complete the structure. For comparison purposes, a similar structure with a single lattice-matched quantum well was also grown.

Arrays of 110-μm-wide broad-area diode lasers with different cavity lengths were fabricated from each sample. The arrays were fabricated by etching 40-μm-wide grooves on 150-μm centers oriented in a (110) direction through the top contacting layer and a portion of the top cladding layer. Ti/Au stripes were used to individually contact each 110-μm-wide laser. After the samples were thinned to ~ 150 μm and a back Ni/Ge/Au ohmic contact applied, linear arrays with cavity lengths ranging from ~ 300 to 3000 μm were cleaved from each sample. The lasers were then tested with 500-ns current pulses at a repetition rate of 1 kHz.

Values of the threshold current density J_{th} vs length L for lasers from the strained-layer single-quantum-well (SQW) and three-quantum-well (3QW) samples are shown in Figure 1-1. Also shown are the J_{th} vs L obtained on the sample with a single lattice-matched quantum well. Results for $J_{th} > 100$ A/cm^2 are not shown but implied by the dashed lines. The J_{th} values obtained with the strained-layer SQW are about half those obtained with the lattice-matched SQW material, confirming the advantages of using biaxially compressed quantum wells. As expected for short cavity lengths, the strained-layer 3QW devices had lower J_{th} than the strained SQW devices, while for longer lengths the SQW devices had lower J_{th}. The SQW devices with 2.6-mm-long cavities had J_{th} as low as 210 A/cm^2, while the 3QW devices with 3.0-mm-long cavities had J_{th} of ~ 260 A/cm^2. Plots of J_{th} vs $1/L$ indicate that the SQW and 3QW devices have transparency currents J_0 of approximately 100 and 210 A/cm^2, respectively.

The reciprocal of the total differential quantum efficency, $1/\eta$, vs L is shown in Figure 1-2. By assuming the loss is independent of current density J (which is probably not as good an approximation for 1.3-μm SCH quantum-well devices as it is for shorter-wavelength AlGaAs diode lasers), an estimate of the total loss α and internal differential quantum efficiency η_i can be obtained from the slope and intercept of these results. For the 3QW material, α and η_i obtained in this way are ~ 4.3 cm^{-1} and 0.7, respectively, while for the strained SQW material they are ~ 3.6 cm^{-1} and 0.65, respectively. A facet reflectivity of 0.29 was used in calculating α.

An estimate of the modal gain G vs J obtained from the J_{th} and η values, assuming $G = (\eta_i/\eta)\ln(1/R)/L$, is shown in Figure 1-3. The results can be fitted to $G = G_0\ln(J/J_0)$, where G_0 and J_0 are 13 cm^{-1} and 100 A/cm^2, respectively, for the strained SQW material, and 35 cm^{-1} and 210 A/cm^2, respectively, for the 3QW material. The J_0 values used to fit the gain are the same as those obtained from J_{th} vs $1/L$.

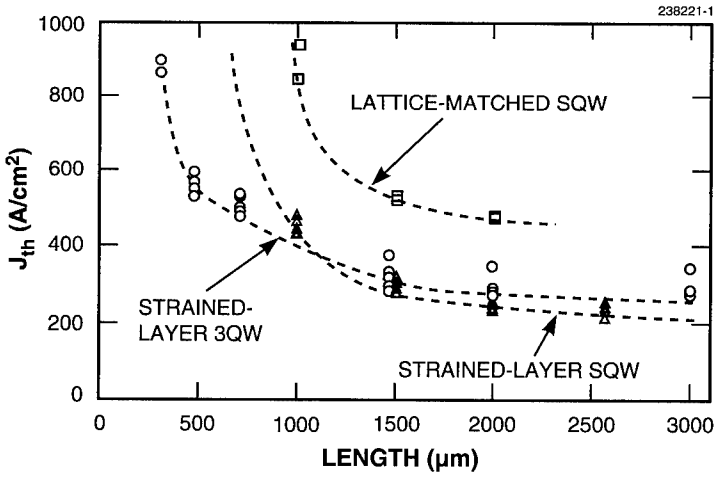

Figure 1-1. Threshold current density J_{th} vs cavity length for broad-area (110-μm-wide) devices. Open triangles and circles are for strained-layer single-quantum-well (SQW) and three-quantum-well (3QW) devices, respectively. Open squares are for devices with a single lattice-matched quantum well.

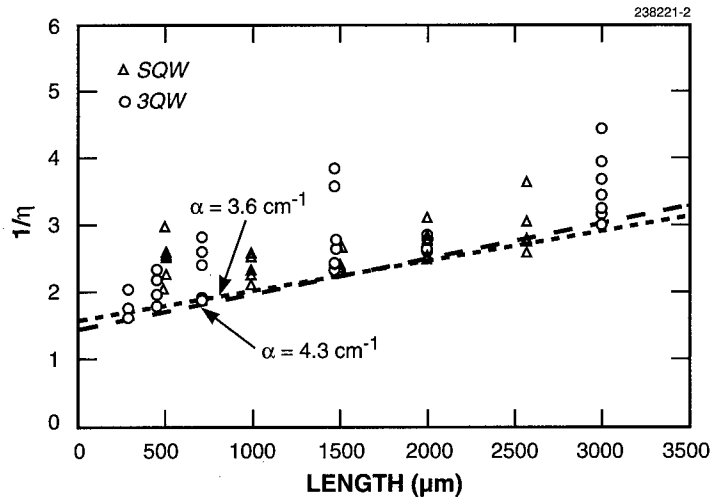

Figure 1-2. Inverse of total differential quantum efficiency vs cavity length for strained-layer devices, following the assigned symbols of Figure 1-1. For SQW devices, these results have been interpreted to give total loss and internal differential quantum efficiencies of α = 3.6 cm^{-1} and η_i = 0.65, respectively. For 3QW devices, values of α = 4.3 cm^{-1} and η_i = 0.7 are found.

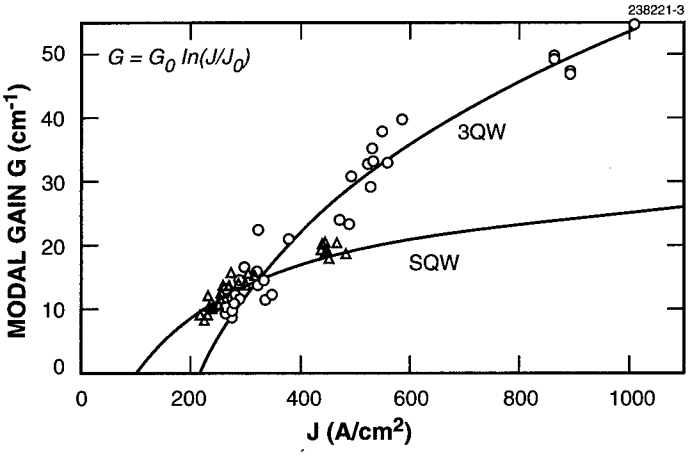

Figure 1-3. Modal gain vs current density J for strained-layer devices. The solid lines fitted to these results are of the form $G = G_0 ln(J/J_0)$, where G_0 = 13 cm^{-1} and J_0 = 100 A/cm^2 for the SQW devices, and G_0 = 35 cm^{-1} and J_0 = 210 A/cm^2 for 3QW devices.

The J_{th} and η values obtained on these strained-layer quantum-well lasers are among the best reported to date in the InGaAsP/InP material system [2], indicating that the OMVPE chimney-geometry reactor is capable of growing high-quality InGaAsP quantum-well structures. Further improvements should be possible using stepped- or graded-index SCH structures to enhance carrier transport and confinement.

J. P. Donnelly
R. J. Bailey
J. D. Woodhouse
S. H. Groves
A. Napoleone

1.2 HIGH-SPEED HIGH-DENSITY PARALLEL FREE-SPACE OPTICAL INTERCONNECTIONS

A dense parallel-array optical interconnection with between 5 and 20 individually addressable elements, a range of several millimeters, and a speed of greater than 1 Gbps has numerous applications. It is useful in supercomputers, high-performance mainframes, multiprocessors, and other digital systems for transferring data between chips in multichip modules or between boards. Here, we extend the concepts used in earlier work on efficient single-element high-speed free-space board-to-board optical interconnection modules [3]. Computers commonly require the transfer of 16-, 32-, 64-, or 128-bit-wide signals. One way this transfer can be accomplished is by multiplexing many lines onto one optical link. Multiplexing would be sensible for an expensive optical technology provided that the data rates are lower than the speed of the optical link divided by the multiplexing ratio. The transfer can also be accomplished with a low-cost optical technology, with parallel arrays of interconnections in which the cost of packaging can be divided by many elements.

Optical fiber communication technology is well established but too expensive and has too much delay for most applications within a computer. One approach toward a low-cost technology is to optimize optoelectronic components for communication over short distances rather than adapt technologies developed for long-distance fibers. Laser drivers, output power monitoring photodiodes, and current-control feedback used for long-distance systems can be eliminated with efficient low-threshold lasers that can be directly driven by logic. A logic output drive capability of 20–30 mA would allow a laser with a threshold of 5 mA or less to turn on with low delay. Thermoelectric coolers are not necessary with lasers that have low sensitivity to temperature variations. High-gain receiver circuits with long delay times that are susceptible to noise can be replaced by simpler low-gain low-latency receivers if lasers and detectors that have high optoelectronic conversion efficiency are used.

Free-space optical transmitter and receiver modules with linear arrays of components have been assembled. The components include 980-nm strained-layer InGaAs laser arrays with double quantum wells [4], glass microlens arrays [5], InGaAs/InP photodiode arrays, and GaAs heterojunction bipolar transistor amplifier arrays [6]. The 980-nm laser arrays have thresholds of 2–5 mA, a high T_0, and an output linearity that is not sensitive to temperature. A photoformed glass lens array with 120-μm-diam

f/1.25 microlenses on a 150-μm center-to-center spacing was selected for the transmitter to collect and collimate each output of the laser array. The receiver lenses are 135-μm-diam microlenses, also on a 150-μm center-to-center spacing. InGaAs/InP back-illuminated photodiodes were flip-chip mounted onto an array of amplifiers that convert the detector current to a level compatible with emitter-coupled logic. The receiver contains an amplifier stage, a comparator stage, and an output level shift stage. Details of the amplifier circuit can be found elsewhere [6].

Transmitter modules with 20 lasers and lenses, and receiver modules with 20 detectors, amplifiers, and lenses, have been assembled. The edge-emitting lasers are mounted for vertical emission perpendicular to boards. The components within the modules are aligned to several-micrometer accuracies. The assembled modules need only be aligned within the system to a lateral accuracy of $\pm$ 22.5 μm to prevent cross talk from becoming an issue. Experimentally, with a single channel, we have observed low bit-error rates over a $\pm$ 40-μm misalignment range, as shown in Figure 1-4. The transmitter can only be tilted a few tenths of a degree, while the receiver can be tilted several degrees before there is a problem. All of these tolerances do not impose any additional requirements and are compatible with advanced electrical packaging already in use for supercomputers.

The output of one of the transmitter elements is shown in Figure 1-5 as a function of laser bias current. The output is over 6 mW at a current of 30 mA, even with a partial high-reflectivity coating on the front facet of the laser. The laser threshold is only 2 mA. The output power of the module does not vary significantly over a range of $\pm$ 10°C around the intended system temperature of 30°C. The uniformity of outputs of seven different channels is shown in Figure 1-6. The lasers in this module have a normal reflectivity so that the efficiency is somewhat higher than for the laser in Figure 1-5, although the thresholds are between 3 and 4 mA.

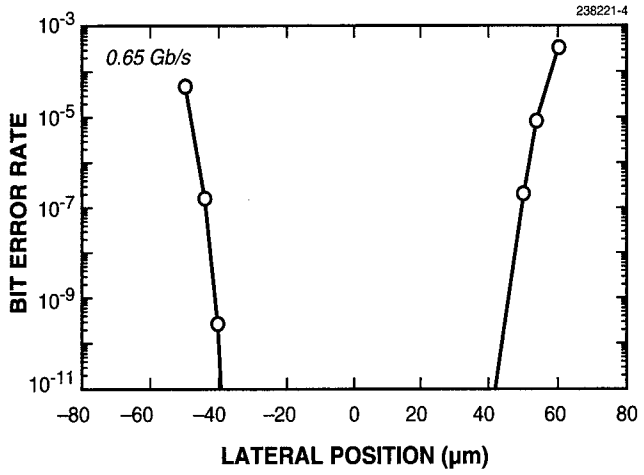

Figure 1-4. Bit error rate vs lateral misalignment of optical interconnection, showing that the rate is low over an 80-μm range.

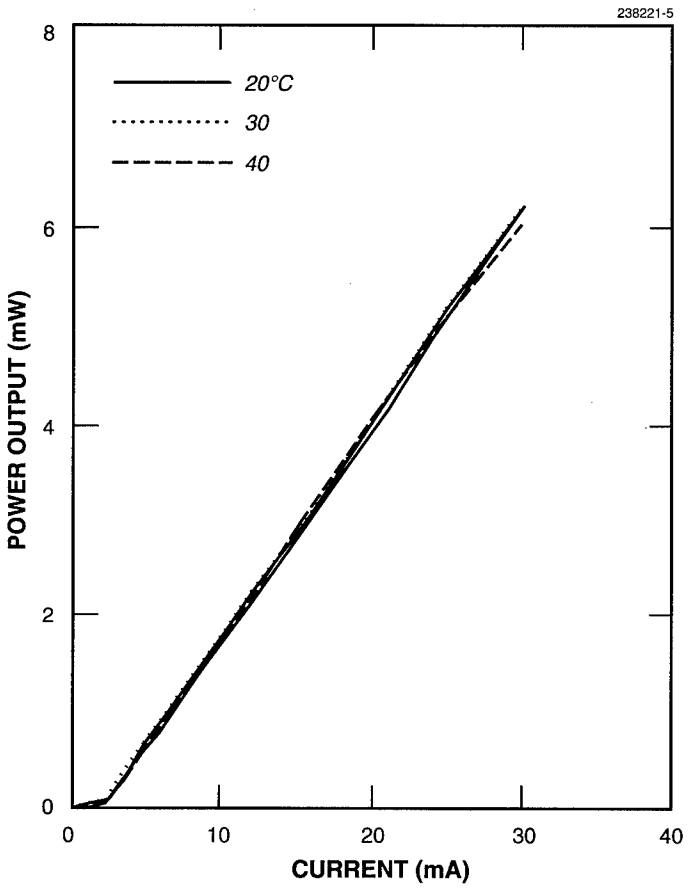

Figure 1-5. Transmitter power output vs laser bias current at temperatures near the intended operating temperature of 30°C.

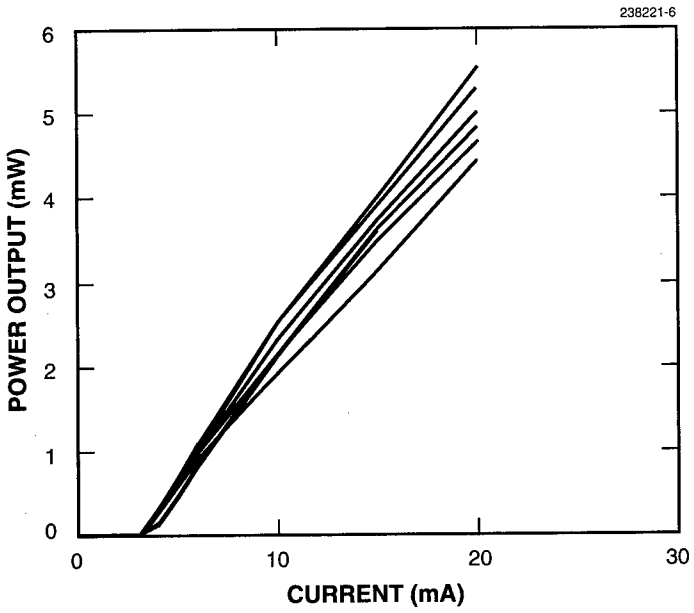

Figure 1-6. Optical power output uniformity of transmitter elements.

The transmitter and receiver modules are each packaged in a separate high-frequency test fixture. Thermoelectric temperature control was not used. The transmitter was driven with an ~ 28-mA signal by a square-wave generator, a bias tee, and a current probe. The receiver output was sampled with 10× probes that are integrated into the test fixture. The sampling oscilloscope response of one of the channels can be seen in Figure 1-7. The 20–80% rise time is 100 ps, while the fall time is 120 ps. The 1-GHz square wave response of two adjacent channels operating simultaneously is shown in Figure 1-8. No optical or electrical cross talk was observed with the system aligned on the sampling oscilloscope. Network analyzer measurements indicate that the cross talk is 30 dB down at a frequency of 1 GHz.

D. Z. Tsang
H. V. Roussell
J. D. Woodhouse
C. A. Wang
J. P. Donnelly
D. L. Spears
R. J. Bailey
J. W. Caunt
D. E. Mull
K. D. Pedrotti*
C. W. Seabury*
R. L. Pierson*

*Author not at Lincoln Laboratory.

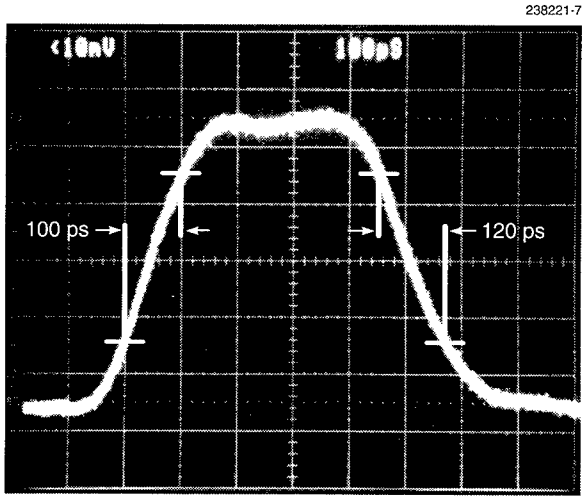

Figure 1-7. Receiver module output waveform. The optical interconnection has 20–80% transition times of 100 ps on the rising edge and 120 ps on the falling edge.

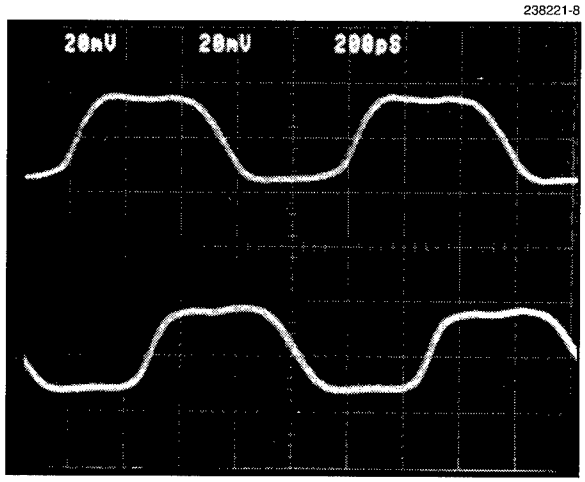

Figure 1-8. Two adjacent free-space optical interconnections operated with 1-GHz clock signals.

REFERENCES

1. S. C. Palmateer, S. H. Groves, J. W. Caunt, and D. L. Hovey, *J. Electron. Mater.* **18**, 645 (1989).
2. A. Mathur, J. S. Osinski, P. Grodzinski, and P. D. Dapkus, *IEEE Photon. Technol. Lett.* **5**, 753 (1993).
3. D. Z. Tsang, *Lincoln Lab. J.* **4**, 31 (1991).
4. Solid State Research Report, Lincoln Laboratory, MIT, 1992:3, p. 8.
5. N. F. Borrelli, D. L. Morse, R. H. Bellman, and W. L. Morgan, *Appl. Opt.* **24**, 2520 (1985).
6. K. D. Pedrotti, C. W. Seabury, R. L. Pierson, and D. Z. Tsang, *Summer Topical Meeting Digest: Hybrid Optoelectronic Integration and Packaging* (IEEE, New York, 1993), p. 8.

2. QUANTUM ELECTRONICS

2.1 2.1-μm Ho:YAG LASER PUMPED BY 1.9-μm DIODE LASERS

Diode-pumped solid state lasers at 2 μm have been demonstrated using Tm^{3+}-doped gain media and Tm^{3+}-sensitized Ho^{3+}-doped gain media pumped at 0.79 μm. Both of these lasers have significant drawbacks. The Tm^{3+} systems have high saturation fluence (~ 50 J/cm^2) and thus are prone to damage under Q-switched operation. The sensitized Ho^{3+} lasers have lower saturation fluence but low extraction efficiency under Q-switched operation because of upconversion and stored energy partitioning between Tm^{3+} and Ho^{3+}. Ho^{3+} lasers pumped at 1.9 μm offer the prospect of improved short-pulse performance relative to the other systems because they have the lower saturation fluence of Ho^{3+} and no stored energy partitioning. Reduced upconversion is expected, and the heat dissipated in the gain medium per unit absorbed pump power is reduced by a factor of 3 to 5 based on quantum defect alone. A 2.1-μm Ho:YAG laser operating on the $^5I_7 \rightarrow {}^5I_8$ transition has been demonstrated previously by intracavity pumping with a Tm:YAG laser at 2.01 μm [1] and by pumping with a single GaInAsSb diode laser source at 1.9 μm [2]. Here, we report on power scaling to the 0.67-W level for a Ho:YAG laser pumped by 1.9-μm diode lasers.

A 4%-doped Ho:YAG laser was end pumped by six 1.9-μm diode lasers using angle multiplexing and polarization beam combining. A schematic of the experiment is shown in Figure 2-1. The pump source consists of five InGaAsP diode lasers and one GaInAsSb diode laser. The gain element is a 2-mm-thick Ho:YAG crystal with an antireflection coating on one surface and a highly reflective coating at both the pump and laser wavelength on the other, which allows the pump radiation to be double passed. The output mirror has a radius of curvature of 10 cm, and the cavity length is such that the laser resonator is nearly hemispherical. The output power for the Ho:YAG as a function of incident pump power is shown in Figure 2-2 for 1.9 and 4% transmission output coupling and a heatsink temperature of –53°C. Approximately 65% of the incident pump power is absorbed, which yields a slope efficiency of ~ 35% relative to absorbed pump power. Figure 2-3 shows the output power as a function of the Ho:YAG heatsink temperature at the maximum pump power, with laser operation obtained at temperatures up to 60°C. The output beam is near diffraction limited with a Gaussian intensity profile.

The slope efficiency is significantly less than the quantum defect limited value of 90%. Experiments show that a portion of the discrepancy is due to imperfect overlap between the pumped volume and laser cavity mode, and improved overlap should increase the slope efficiency to > 40%. Another source of the discrepancy may be upconversion because fluorescence at wavelengths shorter than the pump wavelength is observed. In addition, laser oscillation using 8%-doped Ho:YAG was achieved but the performance was much poorer than with the 4%-doped material. Upconversion is expected to be more severe with highly doped material, and thus using lower doping may lead to improved laser performance. To our knowledge, the maximum operating temperature of the laser (> 60°C) is higher than any other Ho^{3+} laser operating on the $^5I_7 \rightarrow {}^5I_8$ transition demonstrated to date, and it indicates that parasitic processes such as upconversion influence laser operation less than in Ho^{3+} materials sensitized with Tm^{3+}.

C. D. Nabors
J. Ochoa
T. Y. Fan
A. Sanchez
H. Choi
G. W. Turner

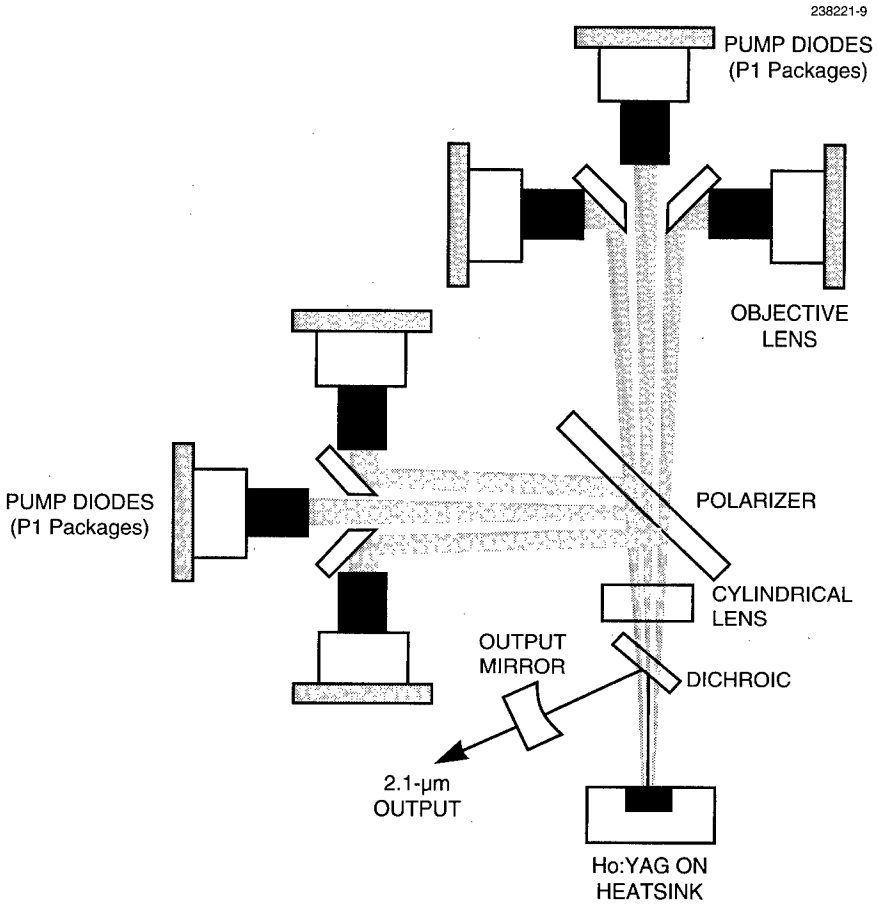

Figure 2-1. Schematic of Ho:YAG laser experiment.

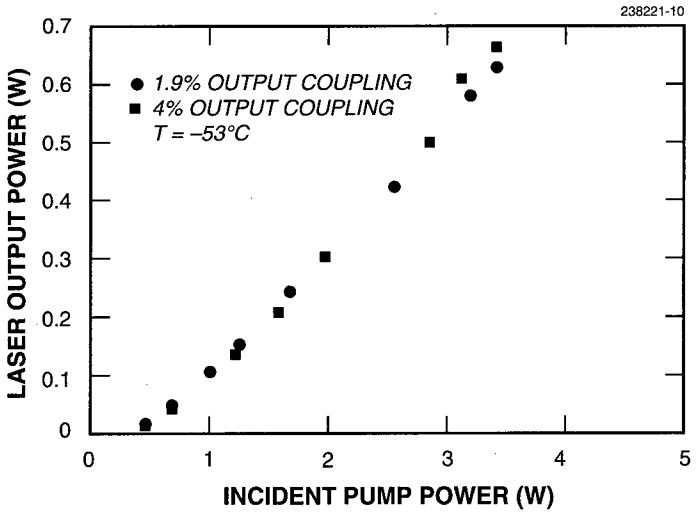

Figure 2-2. Ho:YAG output power at heatsink temperature of –53°C vs incident pump power at 1.9 μm. The output couplings are 1.9 and 4%, and about 65% of the incident pump power is absorbed.

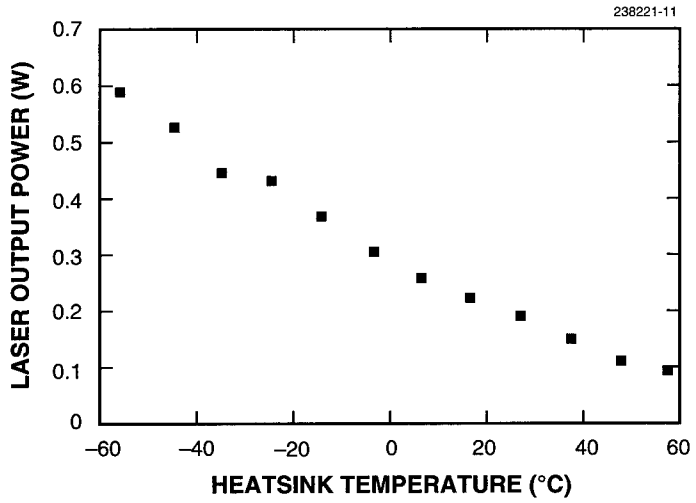

Figure 2-3. Ho:YAG output power vs heatsink temperature at highest pump power for 1.9% output coupling.

REFERENCES

1. R. C. Stoneman and L. Esterowitz, *Opt. Lett.* **17**, 736 (1992).
2. C. D. Nabors, T. Y. Fan, H. K. Choi, G. W. Turner, and S. J. Eglash, *Conference on Lasers and Electro-Optics Postdeadline Papers* (Optical Society of America, Washington, D.C., 1993), Paper CPD8.

3. MATERIALS RESEARCH

3.1 DOUBLE-HETEROSTRUCTURE GaInAsSb/AlGaAsSb/GaSb DIODE LASERS EMITTING AT 3 μm

Semiconductor diode lasers emitting in the mid-infrared (2–5 μm) band are being developed to provide efficient sources for applications such as laser radar, remote sensing, pollution monitoring, and molecular spectroscopy. Diode lasers with GaInAsSb active layers and AlGaAsSb confining layers grown on GaSb substrates are promising for high-performance sources in the 2–5-μm spectrum. For lasers emitting at ~ 2 μm, we have achieved significant improvements in room-temperature performance by employing a GaInAsSb/AlGaAsSb strained-quantum-well active region and AlGaAsSb cladding layers [1],[2]. Broad-stripe lasers have exhibited pulsed threshold current density J_{th} as low as 143 A/cm^2, differential quantum efficiency as high as 70%, and single-ended CW output power as high as 1.3 W. For lasers emitting at 4 μm, double-heterostructure (DH) lasers with a ternary InAsSb active layer and AlAsSb cladding layers have exhibited CW operation at temperatures up to 80 K and pulsed operation up to 155 K [3]. Here, we report the fabrication of DH diode lasers emitting at ~ 3 μm that incorporate a metastable GaInAsSb active layer. These devices, grown by molecular beam epitaxy (MBE) on GaSb substrates, have exhibited pulsed operation at heatsink temperatures up to 255 K and CW operation up to 170 K, with output power of 45 mW/facet at 100 K.

For $Ga_{1-x}In_xAs_ySb_{1-y}$ alloys lattice matched to GaSb substrates, the room-temperature bandgap (wavelength) decreases (increases) steeply from 0.726 to 0.28 eV (1.7 to ~ 4.2 μm) as x increases from 0 to 0.6, but is nearly constant for $0.6 < x \leq 1$ [4]. In terms of valence-band offset and refractive-index step, the best lattice-matched cladding layer available for GaInAsSb is $AlAs_{0.08}Sb_{0.92}$. For $InAs_{0.91}Sb_{0.09}$ ($x = 1$), the valence-band offset with respect to $AlAs_{0.08}Sb_{0.92}$ is ~ 0. Decreasing x increases the valence-band offset, which becomes ~ 0.13 eV for $x = 0.6$. The refractive-index step between $Ga_{1-x}In_xAs_ySb_{1-y}$ and AlAsSb is also larger for smaller x. It is thus advantageous to employ $Ga_{1-x}In_xAs_ySb_{1-y}$ with smaller x for lasers emitting at wavelengths longer than 3 μm.

There is, however, a large miscibility gap for $Ga_{1-x}In_xAs_ySb_{1-y}$, which becomes increasingly less stable as x approaches 0.5. Reported alloy compositions grown by liquid phase epitaxy have been limited to $x < 0.25$ or $x > 0.93$. Metastable alloys of GaInAsSb have been grown by MBE [5] and organometallic vapor phase epitaxy (OMVPE) [6], but they have not been used for lasers.

Metastable alloys 0.9 μm thick were grown by MBE on 1-μm-thick $Al_{0.9}Ga_{0.1}As_{0.08}Sb_{0.92}$ deposited on GaSb substrates. The intended composition of the metastable alloy was $Ga_{0.46}In_{0.54}As_{0.48}Sb_{0.52}$. The x-ray diffraction measurement shows a single peak with a full width at half-maximum (FWHM) of only 37 arc sec, indicating that the material is of good crystalline quality. The photoluminescence (PL) measured at 4.5 K exhibits a strong peak at ~ 3.6 μm with an FWHM of 16 meV. For comparison, the metastable alloy with the largest reported penetration into the miscibility gap is $Ga_{0.4}In_{0.5}As_{0.4}Sb_{0.6}$ grown on InAs by OMVPE, which has a PL peak at 3.5 μm with an FWHM of 3 meV [6].

The laser structure consists of the following layers: 0.5-μm-thick n-GaSb buffer, 3-μm-thick n-$Ga_{0.1}Al_{0.9}As_{0.08}Sb_{0.92}$ cladding, 0.8-μm-thick nominally undoped GaInAsSb active, 3-μm-thick

p-$Ga_{0.1}Al_{0.9}As_{0.08}Sb_{0.92}$ cladding, and 0.05-μm-thick p^+-GaSb cap. The intensity of low-temperature PL is very strong with an FWHM of only 7.5 meV, but the peak wavelength is shifted to ~ 2.9 μm from 3.6 μm for the test layer, corresponding to a bandgap change of ~ 85 meV. This change in PL has been reproducibly observed for three wafers grown under similar conditions. Although we have not investigated the cause for this anomalous bandgap change, it is possible that the atomic rearrangement of neighboring atoms may be responsible. Such rearrangement has been suggested to explain an ~ 50-meV change in bandgap for $In_{0.5}Ga_{0.5}P$ alloys on GaAs grown at different temperatures [7].

Broad-stripe lasers 100 μm wide by 500 μm long were fabricated and mounted p-side up on Cu heatsinks for pulsed measurements and p-side down on diamond submounts on Cu for CW measurements. Figure 3-1 shows the emission spectrum obtained for a laser operating CW at 110 K. It exhibits multiple longitudinal and lateral modes with separations of 2.1 and 0.4 nm, respectively. The peak emission wavelength is 2.97 μm, and it shifts to longer values with increasing temperature at a rate of 1.8 nm/K. The FWHM of the emission is ~ 5 nm.

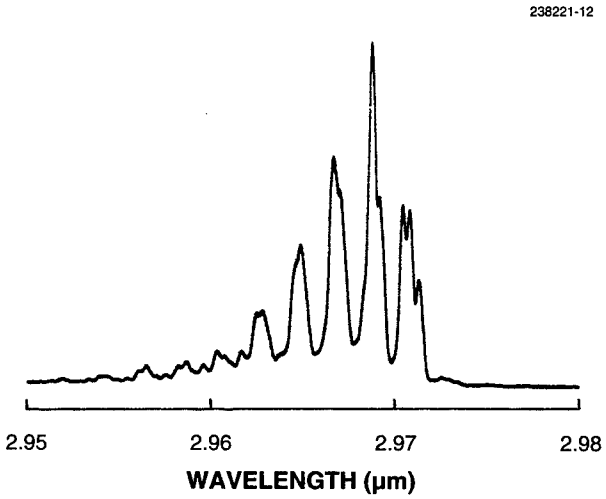

Figure 3-1. Emission spectrum of GaInAsSb/AlGaAsSb diode laser at 110 K.

The pulsed J_{th} for temperatures between 40 and 255 K is plotted in Figure 3-2. The value of J_{th} at 40 K is only 9 A/cm^2. The characteristic temperature T_0 is 35 K for temperatures up to 120 K, and 28 K for higher temperatures. At the maximum operating temperature of 255 K, the value of J_{th} is 13.4 kA/cm^2. These results are significantly better than those for III-V diode lasers emitting between 3 and 4 μm with active layer compositions close to InAs. For such lasers, the maximum pulsed operating temperature is 160 K [8]. The highest operating temperature for any diode lasers emitting at ~ 3 μm was 245 K [9], reported for PbS/PbSrS lasers. The threshold current density at 245 K, however, was more than 50 kA/cm^2.

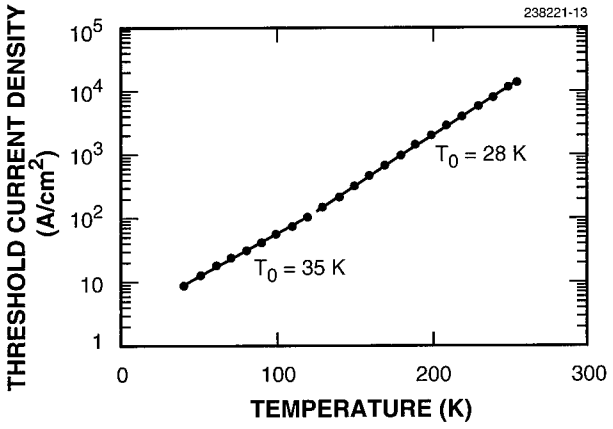

Figure 3-2. Pulsed threshold current density vs temperature for GaInAsSb/AlGaAsSb diode laser.

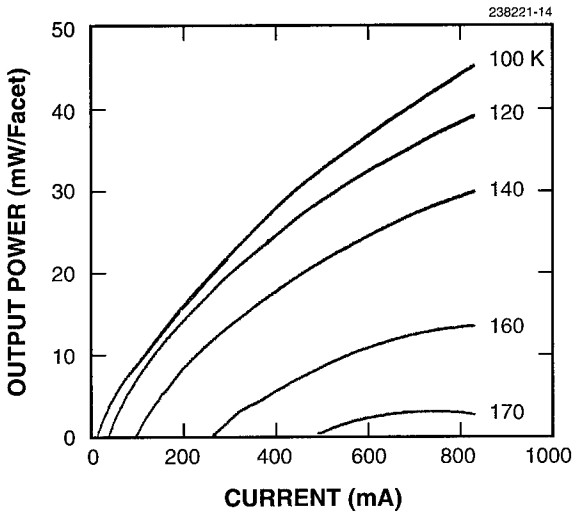

Figure 3-3. CW light output vs current for GaInAsSb/AlGaAsSb diode laser at several heatsink temperatures.

Figure 3-3 shows the CW output power vs current at heatsink temperatures from 100 to 170 K. These curves were obtained by measuring the output with an InSb detector in the linear regime and calibrating it with a thermopile detector. The maximum power at 100 K is 45 mW/facet at 850 mA. The initial differential quantum efficiency at 100 K is ~ 75% from both facets. The laser output power has

been very stable during a few hours of measurement as well as a few times of temperature cycling, even though the active layer is composed of a metastable alloy.

H. K. Choi
S. J. Eglash
G. W. Turner
J. W. Chludzinski
J. V. Pantano
W. L. McGilvary
M. K. Connors

REFERENCES

1. H. K. Choi and S. J. Eglash, *Appl. Phys. Lett.* **61**, 1154 (1992).
2. H. K. Choi, G. W. Turner, and S. J. Eglash, *IEEE Photon. Technol. Lett.* **6**, 7 (1994).
3. S. J. Eglash and H. K. Choi, *Appl. Phys. Lett.* **64**, 833 (1994).
4. J. C. DeWinter, M. A. Pollack, A. K. Srivastava, and J. L. Zyskind, *J. Electron. Mater.* **14**, 729 (1985).
5. T. H. Chiu, Z. L. Zyskind, and W. T. Tsang, *J. Electron. Mater.* **16**, 57 (1987).
6. M. J. Cherng, H. R. Jen, C. A. Larsen, and G. B. Stringfellow, *J. Cryst. Growth* **77**, 408 (1986).
7. M. Kondow, H. Kakibayashi, S. Minagawa, Y. Inoue, T. Nishino, and Y. Hamakawa, *Appl. Phys. Lett.* **53**, 2053 (1988).
8. M. Aidaraliev, N. V. Zotova, S. A. Karandashev, B. A. Matveev, N. V. Stus', and G. N. Talalakin, *Sov. Tech. Phys. Lett.* **15**, 600 (1990).
9. A. Ishida, K. Muramatsu, H. Takashiba, and H. Fujiyasu, *Appl. Phys. Lett.* **55**, 430 (1989).

4. SUBMICROMETER TECHNOLOGY

4.1 PRESHAPING PHOTORESIST FOR REFRACTIVE MICROLENS FABRICATION

Coherent, high fill factor, broadband microlens arrays are needed for such applications as focal plane arrays, optical interconnects, and layered imaging systems. Imaging systems, in particular, require uniform elements with good optical performance, but it is difficult to fabricate uniform arrays of high-quality refractive microlenses for use in the visible, especially with apertures ≥ 100 μm. The fabrication of microlens arrays by melting photoresist cylinders to form spherical lenses, first demonstrated by Popovic et al. [1], has become a widely accepted technique. While optimized processing parameters have been determined for fabricating high-quality 200-μm-diam *f*/2 lenses [2], slower lenses with the same aperture exhibit many waves of spherical aberration. In this report we describe a technique for preshaping the photoresist prior to heat treatment which enables the fabrication of high-quality *f*/4.5 lenses, thereby extending the range of applications.

The conventional technique for fabricating microlens arrays uses standard photolithographic processes for thick resists and can be described as follows. The substrates are cleaned, spin-coated with hexamethyldisilazane to promote resist adhesion, spin-coated with multiple coats of photoresist to achieve the desired thickness (short bake cycles follow each coat), and then prebaked at 90°C. Substrates are exposed using a contact aligner and then developed in the conventional manner to produce cylinders of photoresist. During subsequent thermal treatment in a convection oven, mass transport and surface tension mechanisms minimize the surface area of the photoresist to give an approximately spherical shape. The temperature of this thermal cycle must exceed the photoresist glass transition temperature T_g, where the amorphous polymer changes abruptly from a rubbery state to a glassy state. Most positive resists have a T_g between 120 and 160°C. The surface and interfacial tensions modifying the image shape are limited by gravity, the rheological flow properties of the resist resin, and the difference between the resist and substrate surface tension.

The degree of asphericity of the resultant spherical cap depends on the initial photoresist thickness and cylinder diameter, the photolithography parameters, the melt temperature and time, and the substrate material. A series of experiments have been conducted to determine the optimum processing parameters for 200-μm-diam lenslets. A melt temperature of 200°C for 10 min reproducibly minimizes the spherical aberration. Figure 4-1 shows the measured spherical aberration for 200-μm-diam apertures with varying sag height. The figure illustrates that the photoresist reflow technique is most effective for fast optics. In particular, an *f*/2 lens with 20-μm sag exhibits less than 0.1 wave of spherical aberration (i.e., it is an asphere); *f*-numbers less than 2 have only 1 wave of spherical aberration. Detailed examination of the lens profile reveals that lenses slower than *f*/2 are oblate ellipsoids and faster lenses are slightly prolate.

It is reasonable to assume that slower optics might be fabricated if the resist could be preshaped before reflow. One approach would be to directly write the aspherical shape into the photoresist; another is to use multiple masks and exposures to form an aspheric stepped structure. To test the feasibility of the first approach, a polar-coordinate HeCd laser direct-exposure system has been used to fabricate single lenslets with controlled preshaping. The sample is mounted on a rotating stage, and the exposure optics

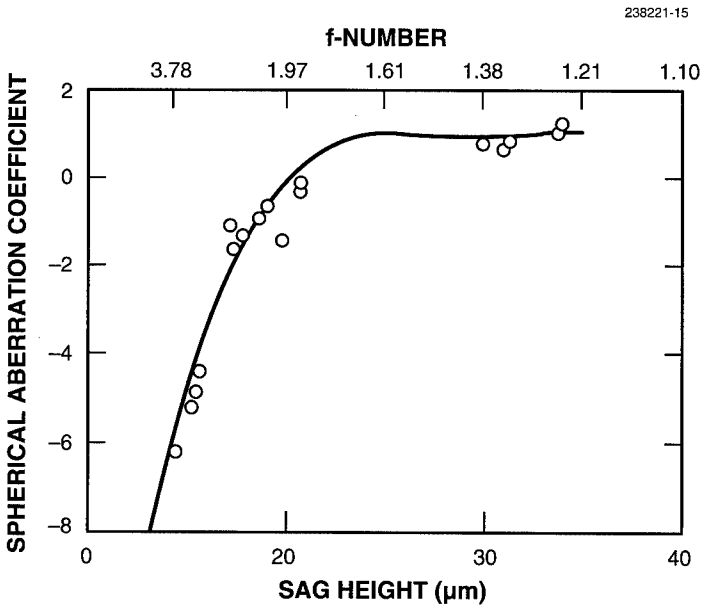

Figure 4-1. Dependence of spherical aberration coefficient on sag and f-number for 200-μm-diam lenslets reflowed at 200°C for 10 min. The spherical aberration for the f/2 lens is less than 0.1 wave.

are mounted on a linear air-bearing stage. A computer controls the intensity and position of the laser beam as it transverses the substrate and exposes the resist. The exposure dose is varied radially across the lens to preshape the photoresist, since the thickness of the photoresist remaining after development is a function of the exposure dose, as shown in Figure 4-2. While it is possible in theory to directly form the photoresist asphere, ridges resulting from the quantization of the radial beam movement result in surface roughness. In addition, an idiosyncrasy of the laser exposure system causes it to initially define a flat-topped central region. These artifacts can be rounded out by thermal reflow, as shown in Figures 4-3(a) and 4-3(b).

Once the basic concept had been proven, a series of experiments were conducted to optimize the thermal cycle. As before, nominally 200-μm-diam lenslets were fabricated and a phase-shifting interferometer was used to measure both the paraxial radius of curvature of each lens and the departure of the lens surface from a sphere. In this case, wavefront deviation was minimized with a 10-min bake at 220°C. By using the preshaping technique, *f*/4.5 optics were fabricated with a spherical aberration coefficient of –0.28, which corresponds to less than a wave of aberration. Figure 4-4 illustrates the completed lens. Without the preshaping technique, our best *f*/3 optics had six waves of aberration, and *f*/4.5 optics would have been much worse.

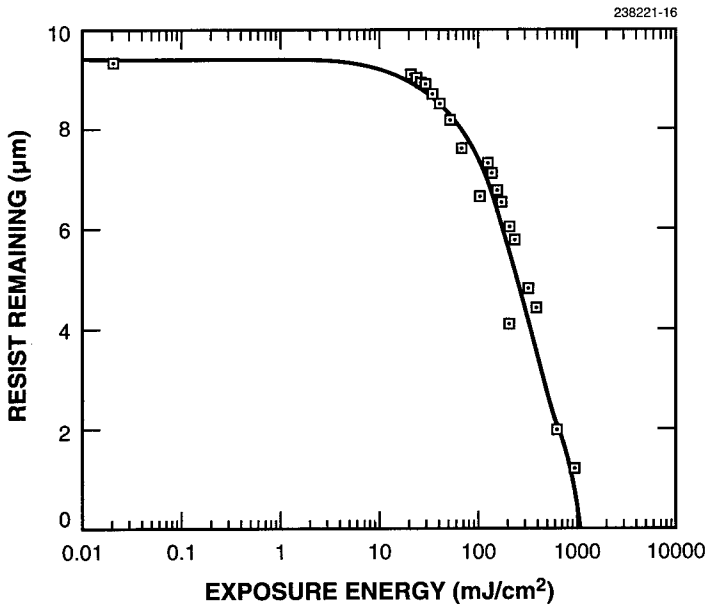

Figure 4-2. Measured contrast curve for AZ4903 photoresist exposed at 442-nm wavelength and developed in AZ421 for 1 min. These results were used to establish the exposure parameters for preshaping the lenses.

The preshaping technique has also been applied to the fabrication of arrays of microlenses. First, stepped aspherical structures were formed by multiple photomasking and contact exposure of the photoresist before development, then the preshaped structures were rounded by thermal reflow. Typical resist profiles are shown in Figures 4-3(c) and 4-3(d), and detailed performance tests indicated that 1.7 waves of spherical aberration was achieved for a 260-μm-diam *f*/3.2 lens with a sag of 15.6 μm. Preshaping the resist profile prior to the reflow, using either technique, dramatically improves the final lens shape.

M. B. Stern
T. R. Jay

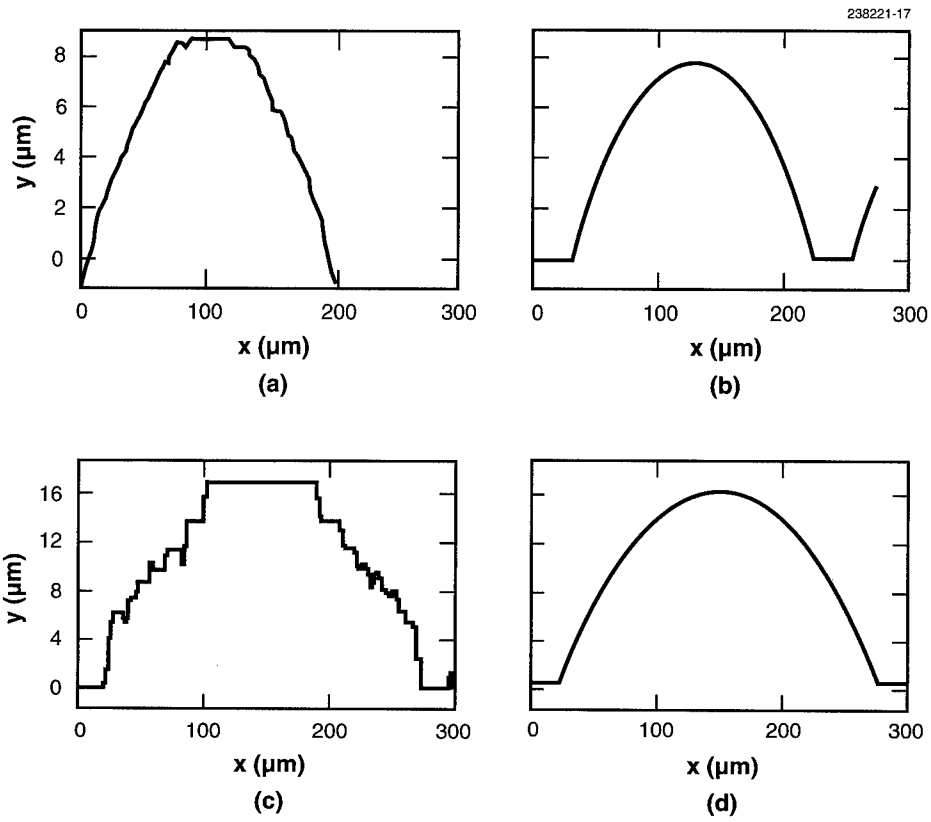

Figure 4-3. Surface profilometer traces of preshaped lenses fabricated using two different techniques. The HeCd laser system was used to preshape the lenses into relatively smooth forms shown (a) before reflow and (b) after reflow. Multiple photomasking results in stepped profiles are shown (c) before reflow and (d) after reflow. In both cases the preshaping rounds the edge of the lens, but the lens does not assume a spherical shape until after reflow. In these traces x is the scan distance and y the height, both in micrometers.

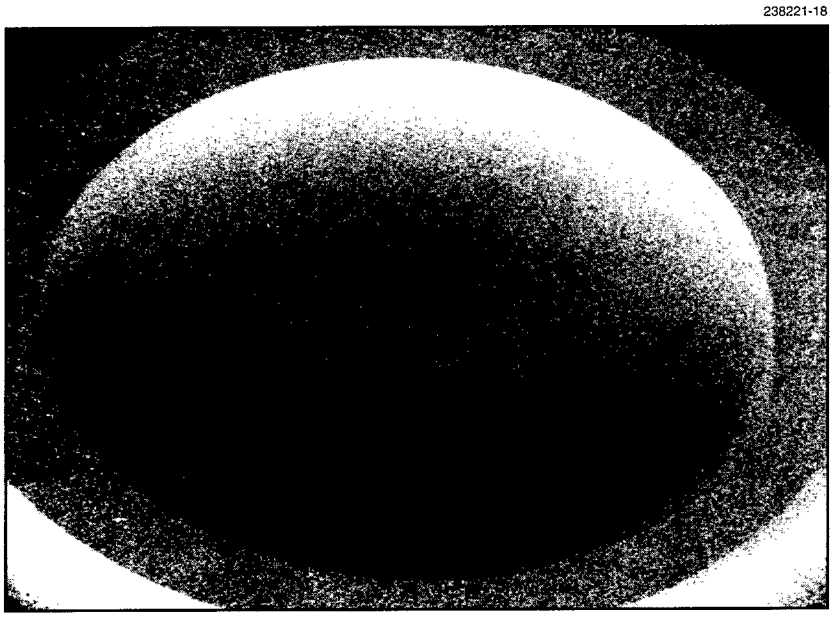

Figure 4-4. Scanning electron micrograph of 200-μm-diam preshaped lenslet after reflow. Thermal treatment at 220°C for 10 min was found to yield the best results.

4.2 ANTIREFLECTIVE COATINGS FOR SINGLE-LAYER 193-nm LITHOGRAPHY

Production photolithography using 248-nm radiation currently faces engineering challenges when patterning nonplanar substrates because of nonuniformities in the photoresist layer thickness. These difficulties stem from thin-film interference in the photoresist. Several years ago Brunner [3] outlined a number of methods for reducing these effects. The methods described were to (1) increase the absorption coefficient α of the photoresist, (2) use an antireflective layer (ARL) on top of the photoresist, (3) use an ARL underneath the photoresist, (4) use a multiple-wavelength exposure, and (5) use high-numerical-aperture optics. For nonbleaching resists used in conjunction with monochromatic (e.g., laser-based) light sources, methods (2) and (3) have been considered the most practical approaches for reducing the effects of standing waves. This report describes the design of an antireflective coating that can be applied beneath a chemically amplified 193-nm resist.

Extensive experimental and modeling work has been done at 248 nm to better understand the requirements, limitations, and performance of ARL technology [4]. This framework will have a direct bearing on developments at 193 nm, as most of the modeling can be generically applied to any exposure wavelength. The limitation for 193 nm, however, lies in the knowledge of the optical properties of the materials in use, since few commericially available instruments can measure the complex refractive index at wavelengths < 200 nm.

Two methods were used for determination of the 193-nm complex refractive index N_{193} of various substrate materials, where $N = n_s + i\kappa_s$. The first method used an ArF excimer laser and an ultraviolet (UV) spectrophotometer. The UV spectrophotometer was first employed to determine the α of the material, then the reflectivity of the sample was measured, and these results were used to calculate the complex refractive index. This method was best suited for measurement of relatively opaque materials ($\alpha > 3\ \mu m^{-1}$), which could also be deposited on fused silica substrates in much thinner layers for the spectrophotometry measurements. Alternatively, determinations of complex refractive index were made by using a spectroscopic ellipsometer equipped with a deep-UV option. Although this instrument was capable of measuring both bulk and thin-film materials, the best results were obtained for transparent and semitransparent thin films.

Table 4-1 summarizes the experimental results. It also shows the calculated normal incidence reflectivity at an interface between the listed material and an infinitely thick layer whose index is 1.685 (e.g., photoresist). These results are contrasted to reflection coefficients for 248-nm wavelength. The relative reflection coefficients are a rough indicator of the need for use of reflection suppression measures when patterning such layers. The biggest differences between 193- and 248-nm reflectivity are for materials that are transparent at 248 nm but opaque at 193 nm. In particular, aromatic-containing organic compounds such as novolac show significant increases in reflectivity at 193 nm.

TABLE 4-1

Optical Constants for Various Materials at Both 193 and 248 nm*

Material	n_{193}	κ_{193}	R_{193}	n_{248}	κ_{248}	R_{248}	R_{193}/R_{248}	Ref.
Si	0.88	2.77	0.58	1.68	3.58	0.53	1.09	[5]
Al	0.113	2.20	0.91	0.190	2.94	0.89	1.02	[5]
W	1.31	3.04	0.52	3.40	2.85	0.33	1.61	[5]
Si_3N_4	2.60	0.27	0.050	2.22	0.020	0.022	2.27	—
i-p-Si	2.0	3.0	0.40	3.2	2.1	0.36	1.11	—
n^+-*p*-Si	1.0	2.4	0.48	2.0	3.5	0.48	1.00	—
Novolac	1.36	0.59	0.047	2.1	0.25	0.017	2.76	—
Brewer Omilayer	1.58	0.49	0.023	1.58	0.20	0.005	4.6	—
Teflon AF	1.4	$<10^{-3}$	—	1.35	$<10^{-3}$	—	—	[6]
Polyimide	1.34	0.53	0.042	—	—	—	1.27	—
Polyimide	1.33	0.52	—	—	—	—	—	[7]
Polyimide	1.26	0.50	—	1.7	0.62	0.033	—	[8]

*The *R* columns list the calculated reflectivity at normal incidence of the indicated material at an interface with a material whose index is $N = 1.685$ (i.e., photoresist).

The design approach for the 193-nm ARL (193-ARL) involved use of a transparent, aliphatic polymer matrix in a phase-compatible blend with an aromatic polymer dye. There were several considerations involved in the determination of this design approach, the most important of which was that monomeric dyes were to be avoided to minimize any possible interdiffusion between the ARL and the chemically amplified resist, which may be prone to poisoning. To permit design simplicity, we chose polymer blends between novolacs and methacrylates. These blends have been reported as highly phase compatible and have successfully been used as i-line, deep-UV, and x-ray resists [9]. To prevent dissolution of the ARL during the spin casting of the photoresist, the methacrylate component contains an epoxide crosslinker. The typical composition contains a copolymer between poly(methylmethacrylate) (MMA) and poly(dicyclopentadienyloxy methacrylate) (DCPOMA) in a blend with novolac. The epoxy group induces crosslinking when heated in the presence of phenolics; the exact structure and concentration of this group dictate the amount of annealing necessary for complete insolubilization. The bake conditions required to render a P(MMA-*co*-DCPOMA)/novolac blend insoluble in propylene glycol monomethylether acetate are 180°C for 10 min.

The blending approach offers a simple means to control the net refractive index of the ARL. The N_{193} is plotted as a function of weight percent novolac in Figure 4-5. The open and filled symbols are results using the reflectivity method and the spectroscopic ellipsometer, respectively. The solid lines connect the data points obtained from the reflectivity results and are provided to guide the eye. It is apparent that the ellipsometer and the reflection method showed some disagreement for strongly opaque materials. In this regime the method of calculation with the ellipsometer uses a bulk model rather than a thin-film model, which may explain the discrepancy.

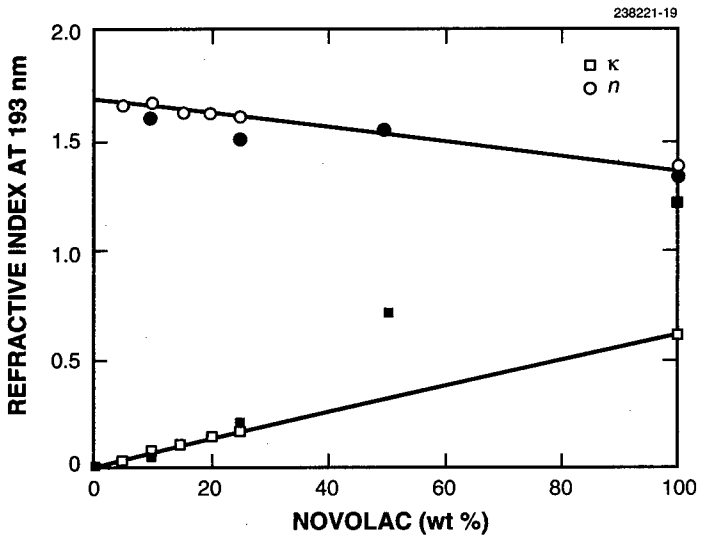

Figure 4-5. Real (circles) and imaginary (squares) parts of refractive index at 193 nm of a P(MMA-co-DCPOMA)/ novolac polymer blend as measured by the reflectance method (open symbols) and spectroscopic ellipsometry (filled symbols).

An ARL polymer blend whose composition is 40-wt% novolac has $N_{193} = 1.56 + i0.26$. Figure 4-6 shows the reflectivity of a resist/ARL stack vs ARL thickness using this index value for the 193-ARL and assuming 700 nm of resist having $N_{193} = 1.685 + i0.006$. A similar curve is given for an ARL whose index is equal to that of novolac, $N_{193} = 1.36 + i0.59$. It is now quite obvious that simple aromatic resins are not acceptable for use as ARL materials for 193 nm because the reflectivity is too high (5%). In Figure 4-7 these sample refractive-index values were used to plot the resist absorption swing curve for an existing chemically amplified resist [10] whose $N_{193} = 1.685 + i0.006$. The three curves in Figure 4-7 are for the resist on Si, resist on novolac/Si, and resist on 193-ARL/Si. Imaging experiments performed over topography using each of these three conditions were carried out on a 0.22-numerical-aperture 193-nm stepper, and the results are shown in Figure 4-8. For the experiments using the novolac and 193-ARL, the ARL was not removed, and hence the underlying topography is not clearly visible. In each case the underlying layer was ~ 200 nm and the underlying topography consisted of 500-nm-high poly-Si steps. It is evident from Figures 4-6 through 4-8 that ARLs are required for these 193-nm resists. Furthermore, the improved linewidth uniformity as seen in Figure 4-8 clearly indicates that our optimized ARL performs significantly better than the alternative we have tried, i.e., novolac. The development of this spin-on material and the extension of existing 248-nm dry-deposited ARLs to 193 nm should allow for either spin-on or dry-deposited antireflection coatings for 193-nm lithography.

R. R. Kunz
R. D. Allen*

REFERENCES

1. Z. D. Popovic, R. A. Sprague, and G. A. N. Connell, *Appl. Opt.* **27**, 1281 (1988).
2. T. R. Jay, M. B. Stern, and R. E. Knowlden, *Proc. SPIE* **1751**, 236 (1992).
3. T. A. Brunner, *Proc. SPIE* **1466**, 297 (1991).
4. T. Ogawa, M. Kimura, T. Gotyo, Y. Tomo, and T. Tsumori, *Proc. SPIE* **1927** (Pt 1), 263 (1993).
5. E. D. Palik, *Handbook of Optical Constants* (Academic, New York, 1985).
6. M. Rothschild, unpublished.
7. A. Yen, H. I. Smith, M. L. Schattenburg, and G. N. Taylor, *J. Electrochem. Soc.* **139**, 616 (1992).
8. E. T. Arakawa, M. W. Williams, J. C. Ashley, and L. R. Painter, *J. Appl. Phys.* **52**, 3579 (1981).
9. R. D. Allen, Q. P. Ly, G. M. Wallraff, C. E. Larson, W. D. Hinsberg, W. E. Conley, and K. P. Muller, *Proc. SPIE* **1925**, 246 (1993).
10. R. R. Kunz, R. D. Allen, W. D. Hinsberg, and G. M. Wallraff, *Proc. SPIE* **1925**, 167 (1993).

---

*Author not at Lincoln Laboratory.

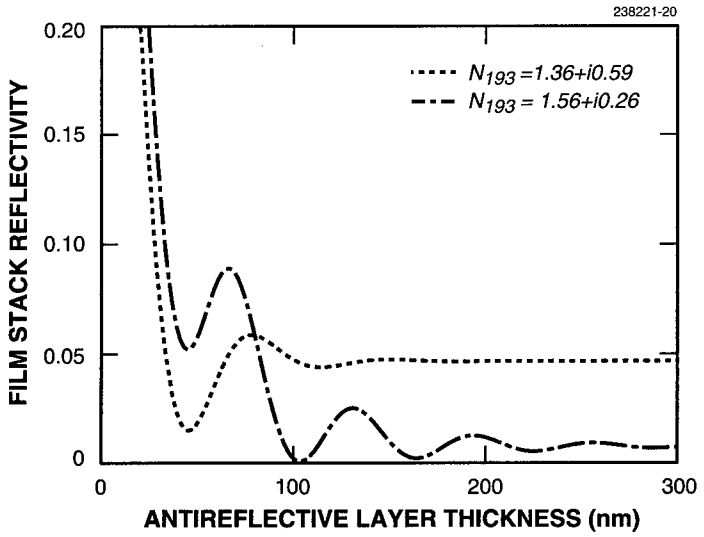

Figure 4-6. Calculated reflectivity vs antireflective layer (ARL) thickness for novolac (N_{193} = 1.36 + i0.59) and 193-nm ARL (N_{193} = 1.56 + i0.26) when used in conjunction with 700 nm of resist whose index is 1.685 + i0.006. These simulations represent the experimental conditions for images found in Figure 4-8.

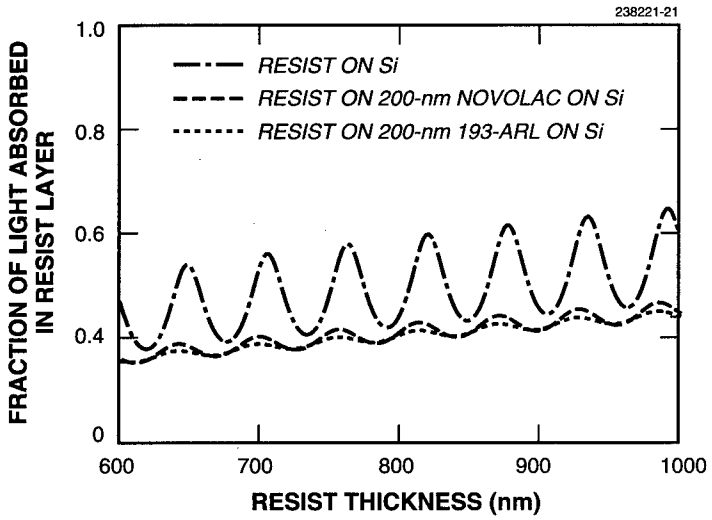

Figure 4-7. Calculated resist absorption swing curves for resist on silicon, resist on 200-nm novolac on silicon, and resist on 200 nm of 193-nm ARL (193-ARL) on silicon. The resist refractive index used was 1.685 + i0.006. These calculations represent the experimental conditions used in Figure 4-8.

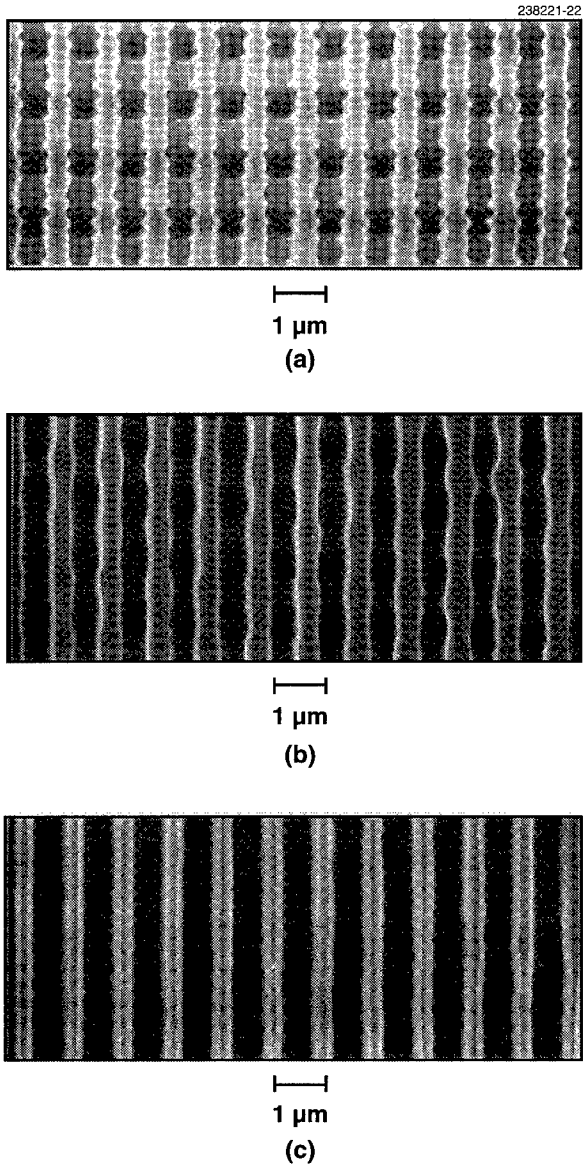

Figure 4-8. Electron micrographs of 0.5-µm images printed over 0.5-µm steps using (a) no ARL, (b) 200 nm of novolac, and (c) 200 nm of 193-ARL. Note that transfer of the resist pattern through the ARL was not performed.

5. HIGH SPEED ELECTRONICS

5.1 OPTICAL-HETERODYNE GENERATION IN LOW-TEMPERATURE-GROWN GaAs UP TO 3.8 THz

The technique of optical heterodyne, or photomixing, of two different laser frequencies has been demonstrated in the past, but because of limitations on the ruggedness and speed of available photomixers it has always been limited to low output powers and < 100-GHz frequencies. This work concerns a new photomixer based on a superior type of photoconductive material—low-temperature-grown (LTG) GaAs [1]. The LTG GaAs is unique in that it exhibits a very short photoconductive lifetime ($\tau < 1$ ps), a high electrical breakdown field ($E_B > 5 \times 10^5$ V cm^{-1}), and a high photocarrier mobility relative to materials having a comparable lifetime. As such, LTG GaAs is capable of withstanding the optical pump powers and bias voltages required to achieve milliwatt levels of CW output power up to frequencies approaching 1 THz.

Our LTG GaAs is grown by molecular beam epitaxy at a temperature in the range 180–240°C and in the presence of arsenic overpressure in the growth chamber. The resulting material is nonstoichiometric with about 1.0% excess arsenic. After growing ~ 1 μm of material, the gallium source is closed. A thermal anneal is then carried out at ~ 600°C in the arsenic flux for a duration of 10 min. The thermal anneal causes the large concentration of excess arsenic atoms to rearrange either as antisite defects (i.e., an arsenic atom at a gallium site) or to cluster together as metallic arsenic precipitates. The antisite defects and precipitates lead to the very short electron-hole recombination time.

To determine the lifetime, we used the technique of time-resolved photoreflectance depicted in Figure 5-1. This is a pump-probe technique in which the optical pulse train from a mode-locked laser is split into two separate beams. The more powerful, pump beam is directed through an optical delay line, mechanically chopped, and then focused on the surface of the LTG-GaAs epitaxial layer where it excites electron-hole pairs. The probe beam is focused onto the same spot as the pump beam, and the average power of the reflected probe beam is measured with a slow photon detector, as the delay line varies the optical path length of the pump beam or, equivalently, the time delay of the probe beam with respect to the pump beam. The photon detector is connected to a lock-in amplifier synchronized at the chopper frequency, so that the output signal of the lock-in amplifier is sensitive only to changes in the reflectivity induced by the pump beam. As the time delay of the pump beam is varied so that the pump and probe pulses arrive at the LTG-GaAs layer simultaneously, the pump has its maximum effect, as shown in the inset of Figure 5-1. As the probe beam is delayed further, the signal strength drops off over a time scale directly related to the lifetime of the photocarriers induced by the pump. The accuracy of this method is limited only by the finite length of the pump and probe pulses, which in our laser is ~ 80 fs.

Using the photoreflectance technique, we determined that the electron-hole lifetime was < 1 ps over the entire growth range of 180–240°C. The most promising material for photomixers was that grown between about 190 and 210°C, for which the lifetime was in the range 0.2–0.4 ps. The minimum lifetime that we observed was 0.15 ps in a sample grown at 195°C. This temperature defines an approximate minimum in the lifetime vs growth temperature.

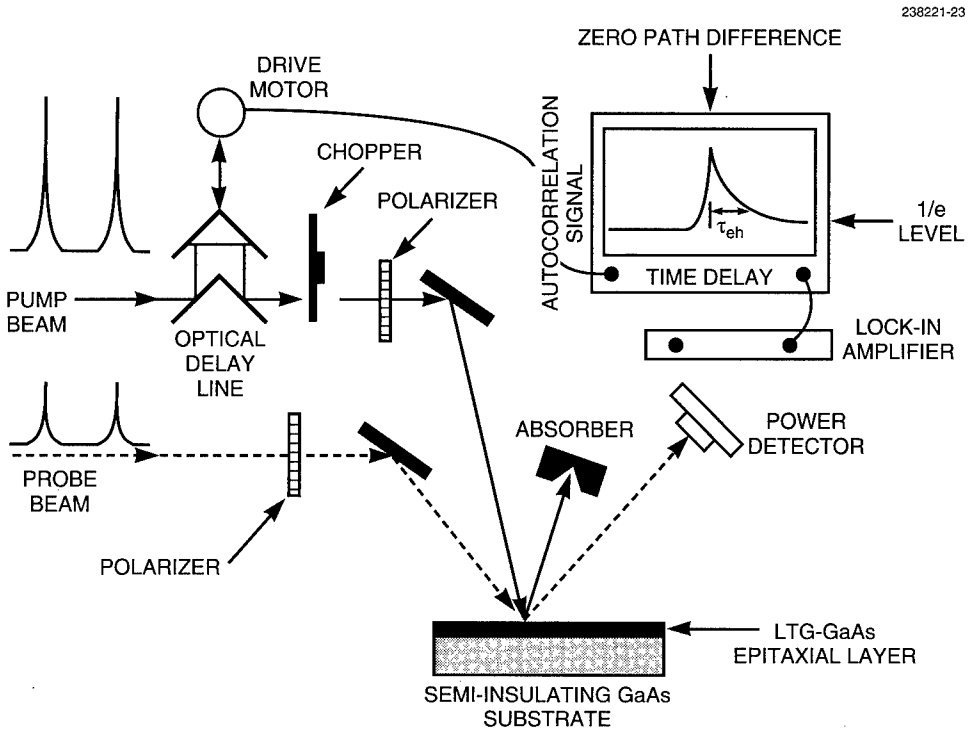

Figure 5-1. Schematic of time-resolved photoreflectance experiment for determining the lifetime of low-tempertaure-grown (LTG) GaAs, with inset showing intensity of reflected probe beam vs time delay between pump and probe beams.

A schematic diagram of the laser pumping configuration used in our experiments is shown in Figure 5-2. It consists of two Ti:Al_2O_3 lasers, each pumped by an argon-ion laser. One of the Ti:Al_2O_3 lasers has a standing-wave optical cavity and is kept at a fixed wavelength of ~ 800 nm over the course of the experiments. The output power is typically in the range 0.1–0.5 W depending on the ion-laser pump power. The output is divided between, at most, two longitudinal modes separated in frequency by 200 MHz. The other Ti:Al_2O_3 laser has a ring cavity with an optical isolator just outside to maintain single-mode, single-frequency operation. The ring laser is tuned continuously in wavelength by a birefringent etalon located inside the cavity. The CW output power of the ring laser is typically in the range 0.2–1.0 W, again depending on the ion-laser pump power.

One of the attractive features of photomixing is that the delicate task of beam combining can now be carried out using fiber-optic components. As shown in Figure 5-2, this is done by first transforming the output beams of the Ti:Al_2O_3 lasers into single-mode fiber using free-space-to-fiber couplers. The two single-mode fibers are connected to a broadband fiber-optic power combiner. Although the combiner is somewhat inefficient (only about 25% of the total input power gets into the output fiber), it is quite

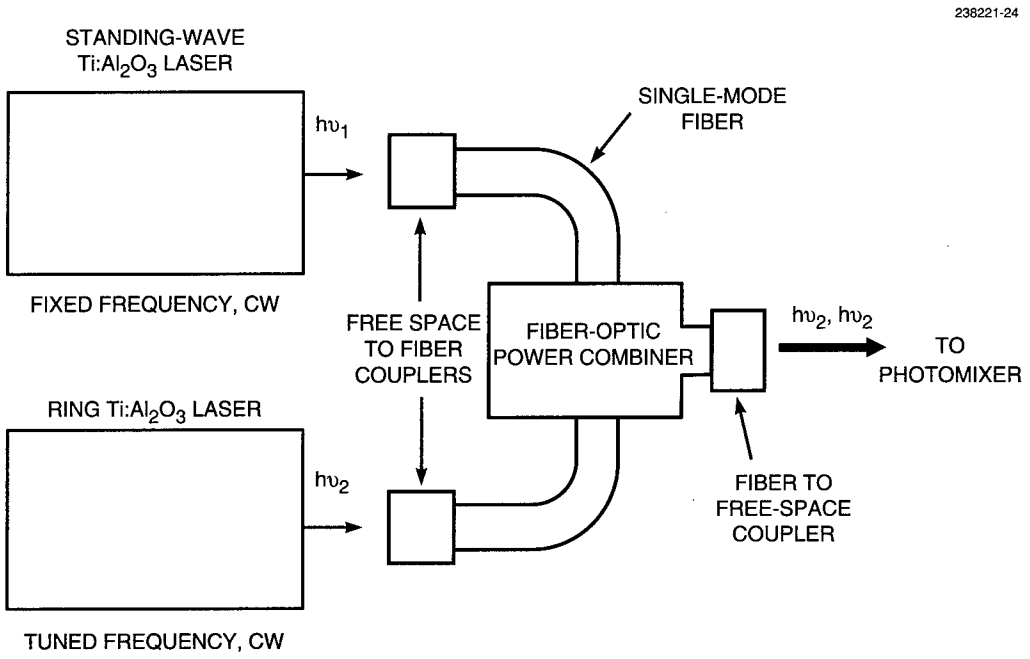

Figure 5-2. Experimental configuration for optically pumping photomixer.

rugged and vibration insensitive compared to any free-space combining technique. After combining, the beams are transformed back into free space and focused on the photomixer active region.

To obtain a photomixer having a sufficiently low capacitance to operate at terahertz frequencies, we have implemented the interdigitated contact structure shown in the representative electron micrograph at the lower right of Figure 5-3. The interdigitated electrodes are fabricated on the top surface of the LTG GaAs by the following steps. First, electron-beam lithography is used to open up channels having the dimension of the desired electrodes in a thin layer of polymethylmethacrylate (PMMA). Then, thin layers of titanium and gold are deposited on the entire pattern. Finally, the metal over the grid of remaining PMMA is lifted off using a chemical solvent.

In operation, the laser beams are focused on the interdigitated-electrode region, generating electron-hole pairs in the LTG-GaAs gaps between the electrodes. The electrons and holes are induced to drift to opposite contacts by a large dc-bias field applied between electrodes. The drifting carriers constitute a photocurrent that has a frequency component at the laser-beam difference frequency $|\nu_2 - \nu_1|$; this component can generate power by driving the characteristic impedance of a transmission line or the radiation resistance of an antenna. We use a 50-Ω coplanar waveguide as the transmission line for difference frequencies from 0.2 to 50 GHz [2]. For higher frequencies, we couple the interdigitated-electrode structure to a self-complementary spiral antenna, as shown in Figure 5-3. The spiral is a type of broad-

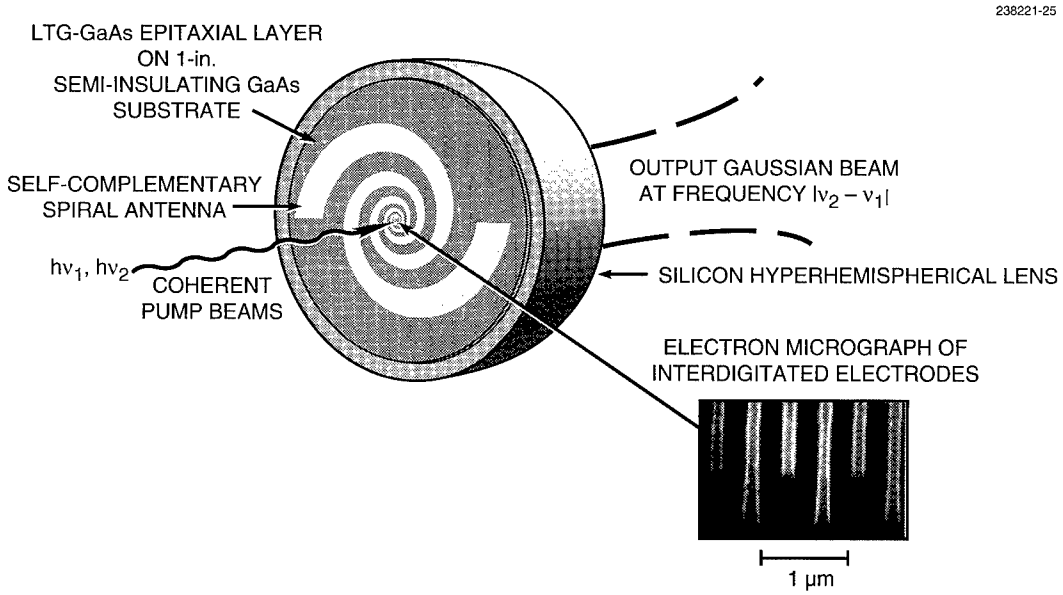

Figure 5-3. LTG-GaAs photomixer with interdigitated-electrode structure coupled to broadband self-complementary spiral antenna and silicon hyperhemispherical lens.

band antenna whose useful range can easily exceed 1 decade of frequency. When lying on a GaAs half-space, its radiation resistance is ~ 72 Ω. The low frequencies radiate from the outer extent of the spiral, and the high ones from the inner. At all frequencies, the majority of the radiation goes into the GaAs substrate because its dielectric constant is much larger than that of free space. The radiation is transformed into free space without significant total internal reflection by abutting the substrate to a silicon hyperhemispherical lens. The radiation coming out of the lens forms a diverging quasi-Gaussian beam, which is easily coupled into other millimeter-wave components and systems.

Our highest frequency measurements have been carried out on an interdigitated structure having eight 0.2-μm-wide electrodes and seven 1.8-μm-wide gaps. The spiral antenna for the high-frequency measurements had two complete turns in each arm with an inner radius of 30 μm and an outer radius of 1.8 mm. These dimensions correspond to a frequency range of approximately 60 GHz to 1.0 THz. The output power from the spiral antenna was measured with a liquid-helium-cooled composite bolometer having high sensitivity throughout the far-infrared region. The output frequency was determined by separately measuring the frequency of each pump laser using an optical wavemeter with an accuracy of ~ 1 GHz.

Figure 5-4 is a plot of the photomixer CW output power as a function of laser difference frequency between 10 GHz and 3.8 THz. The data point at 10 GHz was measured with the photomixer coupled to the coplanar-waveguide structure. The results at higher frequencies were obtained with the spiral-antenna structure. Relative to the 10-GHz point, the output power is approximately constant out to ~ 300 GHz and then rolls off. The 3-dB-down frequency was ~ 500 GHz. The small peak around 800 GHz is thought to represent a transition to dipole radiation by the interconnect metal between the interdigitated electrodes and the inner radius of the spiral. Beyond 1 THz, the output power rolls off somewhat faster than 12 dB/ octave. The rate of 12 dB/octave is what we expect from two time constants operating in the photomixer: the electron-hole recombination time and the electrical RC time. Our LTG GaAs had a photocarrier lifetime of 0.35 ps as measured by the time-resolved photoreflectance technique. Thus, the output power should begin rolling off rapidly at a frequency of $(2\pi\tau)^{-1}$ = 455 GHz, in good agreement with the experiment. For our spiral antenna on a GaAs substrate, R is the driving-point resistance of 72 Ω and C is the interdigitated-electrode capacitance. According to electrostatic theory, the capacitance of this structure is ~ 1.9 fF. Hence, we calculate RC ≈ 0.14 ps and a 3-dB frequency of $(2\pi RC)^{-1}$ = 1.1 THz. The additional experimental rolloff beyond 1 THz is thought to represent the drop in radiation resistance of the dipole with frequency.

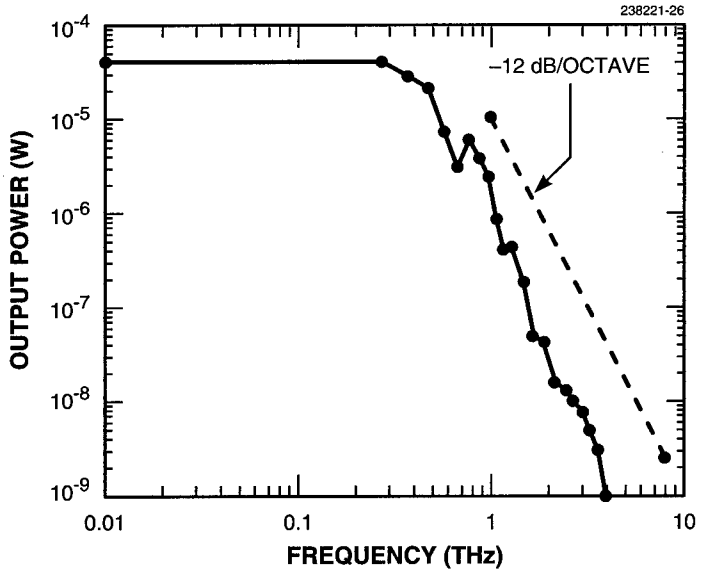

Figure 5-4. Output power vs frequency for LTG-GaAs photomixer coupled to coplanar-waveguide transmission line (10-GHz point) and self-complementary spiral antenna.

Another well-understood aspect of the photomixer performance is the output polarization. Up to frequencies of ~ 300 GHz, the output beam from the spiral antenna is nearly circularly polarized as expected. Above ~ 800 GHz, the output becomes linearly polarized. We believe that this represents a transition from radiation by the spiral to radiation by the dipole-like interconnect metal. Taking the 60-μm length of the interconnect as the physical length of the dipole, we estimate that a half-wave dipole resonance should occur at a frequency of 950 GHz. Between this point and the full-wave resonance, we expect the interconnect to radiate efficiently because the radiation resistance should increase rapidly with frequency.

The radiation generated by the photomixer beyond ~ 2.5 THz represents the highest coherent frequencies ever achieved by electronic or optoelectronic means. The LTG-GaAs photomixer may fill the need for solid state coherent radiation at frequencies > 1 THz, where tunable solid state sources are lacking.

E. R. Brown
K. A. McIntosh
K. B. Nichols
M. J. Manfra
C. L. Dennis

REFERENCES

1. F. W. Smith, Ph.D. thesis, Massachusetts Institute of Technology, 1990.
2. E. R. Brown, K. A. McIntosh, F. W. Smith, M. J. Manfra, and C. L. Dennis, *Appl. Phys. Lett.* **62**, 1206 (1993).

6. MICROELECTRONICS

6.1 ORTHOGONAL-TRANSFER CCD IMAGER

Conventional charge-coupled-device (CCD) imagers, though two-dimensional in structure, are capable of transferring a charge-packet array along only a single dimension. A CCD which can transfer charge in all four directions could find use in imaging applications where the charge would be shifted to track a moving image and thereby eliminate blur. Séquin [1] proposed a structure capable of true two-dimensional transfer which had five clock phases and could be realized with five conductor levels, as well as an alternative version which used only three conductor levels. From a fabrication point of view the former has the virtue of being immune to intralevel gate-gate shorts, but has the drawback of requiring more conductor levels. The latter version, on the other hand, requires gates for separate clock phases to be fabricated on the same conductor level (therefore leaving it vulnerable to intralevel shorts), and in addition requires these gates to be closely abutted. For good charge transfer the gap between these gates must be < 1 μm, and this exacerbates the susceptibility of the structure to intralevel shorts. The only two-dimensional-transfer CCD demonstrated thus far has been a 32 $\times$ 32 device by Kansy [2] that was developed as a reformatting analog memory for two-dimensional Fourier transforms, but his structure allowed only unidirectional transfer in each of two orthogonal directions.

We describe here a new two-dimensional CCD structure, which we term an orthogonal-transfer CCD (OTCCD), that is capable of transferring charge in all four directions. In contrast to Séquin's proposed structure [1], it is implemented as a four-phase device in four conductor levels. It thus features immunity to intralevel shorts with one less level and therefore can be applied to large-area devices with the prospect of high yields. We also describe some initial results on a 64 $\times$ 64-pixel prototype frame-transfer imager in which the OTCCD structure is used in the imaging pixels.

Figure 6-1 illustrates the basic features of the CCD cell, with the four gate levels, or phases, labeled G1–G4. With G1 biased low to act as a channel stop, gates G2–G4 can be clocked in a conventional three-phase manner to transfer charge vertically. Likewise, the gates G2 can be biased low and gates G1, G3, and G4 can be clocked to transfer charge horizontally. Conventional channel stops (such as LOCOS) are required under the intersection of the G1 and G2 gates and are shown as shaded areas. Figure 6-2 shows a portion of an OTCCD pixel array from the imaging section of a 64 $\times$ 64-pixel frame-transfer imager. The pixel dimensions are 27 $\times$ 27 μm. The gates are fabricated from three levels of polysilicon (G1–G3) and one aluminum level (G4). A more desirable alternative to aluminum would be a fourth level of polysilicon because of the tendency of aluminum to short through thin gate dielectrics.

This device has been tested with an optical input to demonstrate the two-dimensional shifting capability. Figure 6-3 illustrates the results on one such test, in which a laser was focused within a pixel near the center of the imaging array. The laser wavelength was 543 nm, and the device was at room temperature. The CCD clocks were then driven to clock the charge along the closest approximation to one cycle of the curve described by the equation

$$x = k\{2\cos(t) + 3\cos(2t)\} \qquad 0 < t < 2\pi \quad ,$$
$$x = k\{2\cos(t) + 3\cos(2t)\} \qquad (6.1)$$

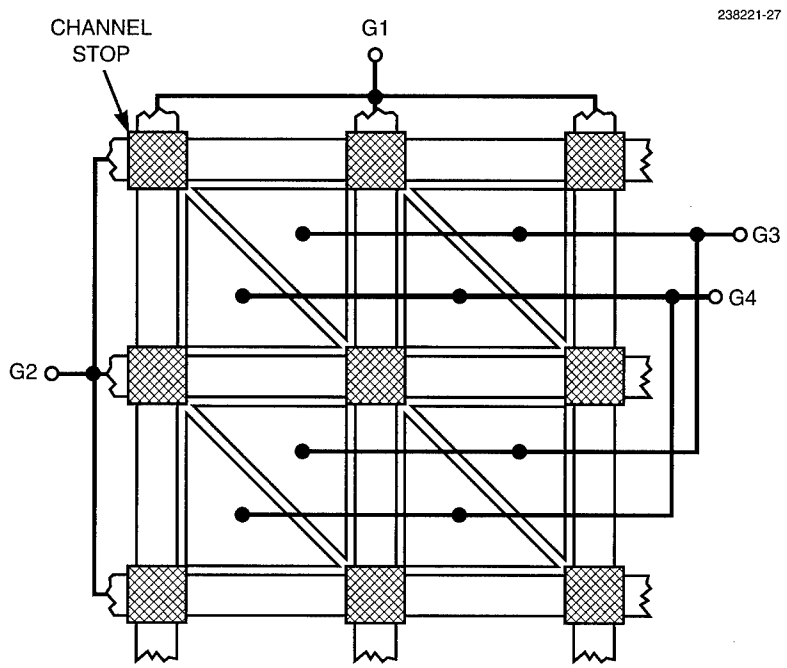

Figure 6-1. Schematic of essential features of the orthogonal-transfer charge-coupled-device (OTCCD) pixel. The device uses four gates levels, denoted G1–G4, and can transfer charge in all four directions.

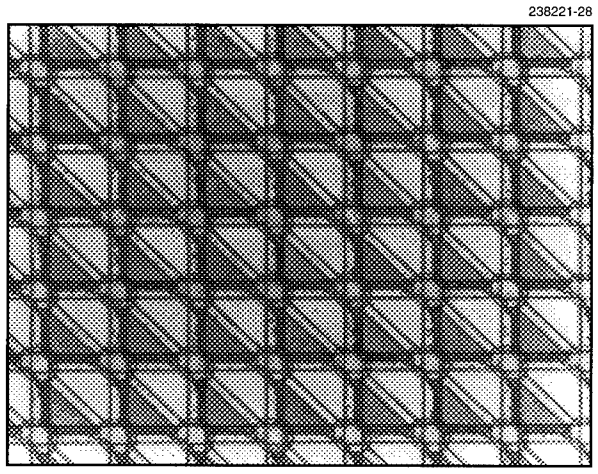

Figure 6-2. Photograph of portion of OTCCD pixel array from a 64 × 64-pixel frame-transfer imager. The gates are fabricated from three polysilicon levels (G1–G3) and one metal level (G4).

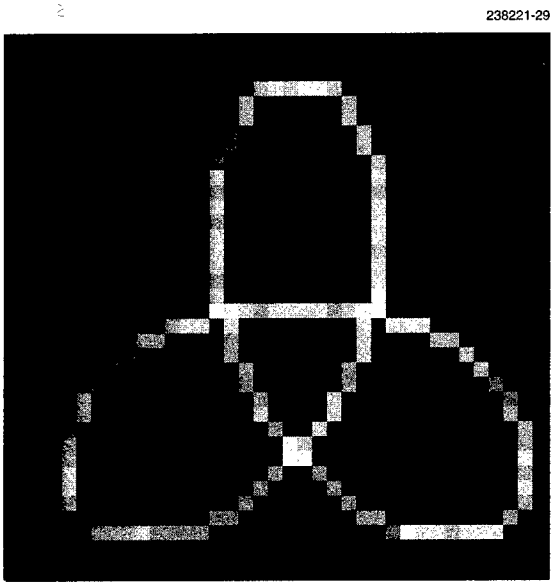

Figure 6-3. Image from OTCCD in which a light spot is focused into single pixel near the center, and the gates shifted to approximate curve described in Equation (6.1).

where k is an arbitrary scaling factor. In this example, the clock period for transferring by 1 pixel was 5.0 μs and for integration on the light spot was 500 μs. After the curve was completed the charge was quickly shifted to the frame store and read out. The charge-transfer inefficiency appears to be below 10^{-4} per pixel. A more precise number could not be obtained because of the relatively limited number of transfers and because the room-temperature dark current of about 1000 e^-/pixel acts as a "slim zero" and masks charge losses smaller than the dark charge. One application for this device would be in improving the resolution of ground-based astronomical imaging. Atmospheric turbulence produces random phase distortions in the optical wavefront which severely degrade the image resolution to well below the diffraction limit of large telescopes. Much of the distortion manifests itself as a tilt in the wavefront, and this in turn leads to a translation of the image at the focal plane. Conventional adaptive-optics systems compensate for this lowest-order distortion by using a fast tip-tilt mirror in the optical path. An OTCCD could achieve this correction electronically by shifting the charge to maintain registration with the moving image. Mechanical resonances are a challenge for tip-tilt mirrors, but even a large OTCCD with resistive polysilicon gates can easily follow motions at a rate of 1 kHz. As with other systems, the information on the image displacements must be independently measured and processed, usually with a high-frame-rate imager viewing a bright, nearby star, or possibly using a fraction of the light from the object of interest if it is bright enough.

B. E. Burke
E. D. Savoye
T. A. Lind
R. K. Reich
J. L. Tonry*

*Department of Physics, Massachusetts Institute of Technology, Cambridge, Massachusetts.

6.2 CCD DETECTION OF ^{32}P FOR DNA HYBRIDIZATION SEQUENCING

Arrays of CCDs fabricated on high-resistivity bulk silicon substrates have been investigated for sensitive detection of the radioisotope label ^{32}P, commonly used in DNA hybridization sequencing. Collection efficiency of electrons created by an energetic ^{32}P beta particle is improved by deep-depletion detection regions inherent to high-resistivity material. The nominal detection sensitivity of the CCD was found to be 5 to 10 times greater than commonly available gas phase arrays and approximately 2000 times greater than x-ray film. Activity levels ranging over 2 orders of magnitude were detected during a single integration period. The capability of the CCD array for DNA sequencing has been demonstrated by using the array to directly detect ^{32}P-labeled target DNA hybridized by probe DNA.

A 420 × 420-pixel frame-transfer CCD fabricated on a 6000-Ω cm silicon substrate was used to detect the beta particles. The sensitivity of the CCD for beta particle detection depends on the CCD signal generated per event, the CCD detector noise, and the generated electron signal noise. The signal generated per event has been measured at 40 000 electrons (spread over several pixels) by calibrating the CCD response to known quantities of the ^{32}P label. The detector noise is composed of dark-current noise and readout amplifier noise. All measurements were taken at room temperature and used CCD integration times of ~ 1 s, giving 16 000 electrons/pixel generated by the dark current (420 pA/cm^2) and a corresponding shot noise of 130 electrons/pixel per second. The readout noise (< 40 electrons/pixel) under these conditions is considered negligible.

The CCD detection sensitivity to beta particles was evaluated by imaging known quantities of ^{32}P that had been placed on carrier substrates. The substrates were silicon dies, of the same size as the CCD imaging array, that had a grown amorphous silicon dioxide layer on the surface. Three ^{32}P spots with activity levels ranging from 100 to 10 000 decays per minute (DPM) were placed on the carrier substrate and the substrate put on the surface of the CCD. Figure 6-4 shows an image of the electron signal generated by the decay events vs position in the 420 × 420-pixel imaging array after a 30-s integration time. Bright areas in the image represent regions of high beta particle activity. Figure 6-5 is a plot of the summed electron signal and calculated standard deviation vs measured DPM levels for each of the three spots. The results in Figure 6-5 show an approximately linear increase in electron signal with decay rate over the 2 orders of magnitude, demonstrating the dynamic range of the CCD. The lowest decay rate sample of 100 DPM was used to compare measurement techniques. The number of counts detected using the CCD after a 2-min integration was 120 at an S/N ratio of 10. The same samples measured on a gas-phase array required an acquisition time of ~ 20 to 30 min to obtain a similar signal-to-noise (S/N) ratio, while x-ray film needed hours.

An attempt at DNA sequencing by hybridization was made using the CCD direct detection method. Four DNA probes with different 9-mer sequences were linked to the amorphous silicon dioxide layer in separate quadrants. Each quadrant of the carrier substrate contained a 3.5-mm dot of probe DNA. As shown in Figure 6-6, the four 9-mer probes differed by a single base located at the center of its strand. A 21-mer target DNA containing the ^{32}P radioisotope label was applied to the substrate surface. At the center of the target strand was an exact complementary match to one of the probes. The hybridized substrate was placed face to face with the CCD detector array. Figure 6-7(a) shows an image of the

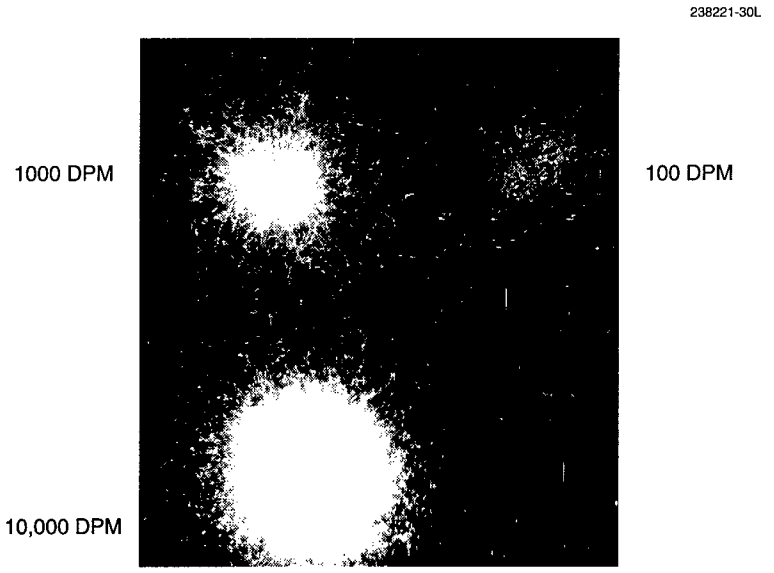

Figure 6-4. 420 × 420-pixel image of four ^{32}P radioisotope label samples. Bright areas are regions of high beta particle activity. DPM is decays per minute.

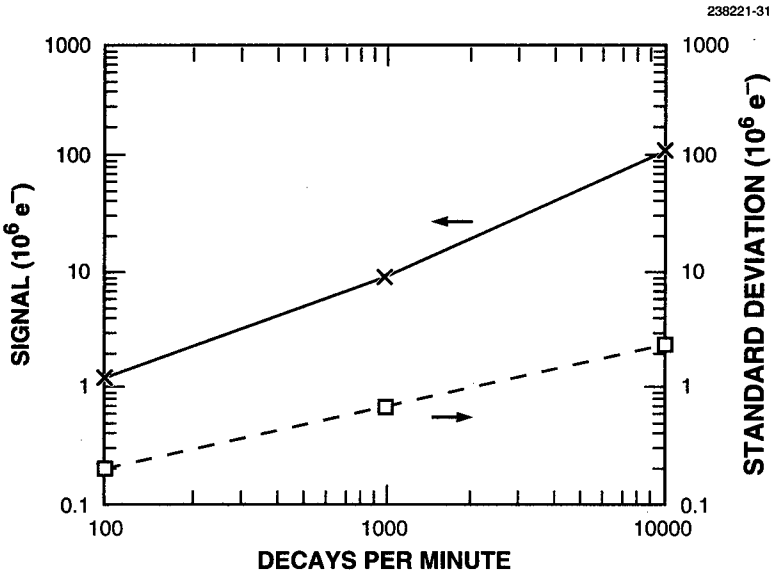

Figure 6-5. Average electron signal and standard deviation vs decays per minute. The average electron signal is found as the sum of the electron signals from the pixels in the region containing the particular sample.

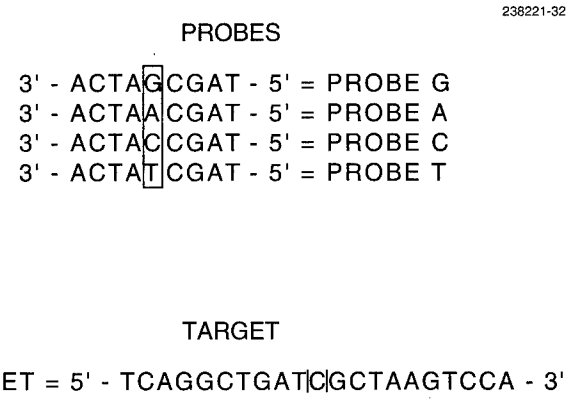

Figure 6-6. Four 9-mer DNA probes showing location where single base is varied. Also shown is the 21-mer target DNA to which hybridization was attempted. The exact matched base pair for the target and probe is C:G.

detected electron signal vs location in the 420 × 420-pixel array. Once again, bright areas in the image indicate high activity levels. The exact matched site is easily distinguished from the mismatched sites. Figure 6-7(b) shows the summed electron signal for each quadrant. As demonstrated in Figure 6-7(b), the matched site has a signal 17 times greater than the other mismatched sites. Also this site had a measured decay rate of 6000 DPM and an S/N ratio of 10, which compare well to the ^{32}P calibration results.

R. K. Reich
M. E. Hogan*
B. E. Burke
E. J. Ehrlich
M. A. Hollis
S. R. Smith*
J. B. Lamture*
K. L. Beattie*
M. D. Eggers*
R. Fowler*
B. B. Kosicki
R. S. Varma*

REFERENCES

1. C. H. Séquin, *IEEE J. Solid-State Circuits* **SC-9**, 134 (1974).
2. R. J. Kansy, *IEEE J. Solid-State Circuits* **SC-14**, 1041 (1979).

*Author not at Lincoln Laboratory.

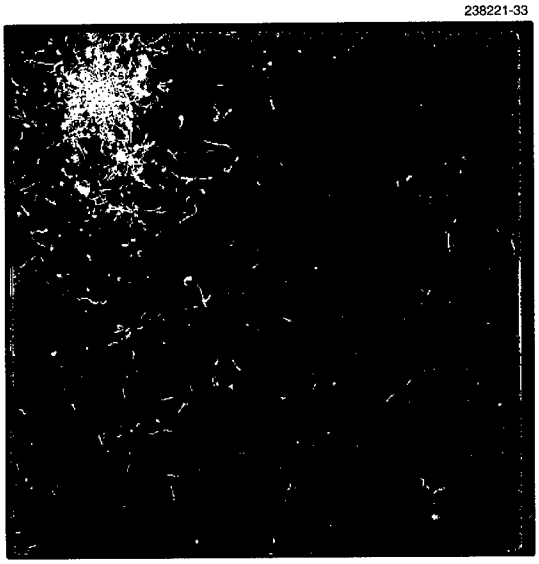

(a)

C:G 9.7×10^6	C:A 5.5×10^5
C:T 3.5×10^5	C:C 2.3×10^5

(b)

Figure 6-7. (a) 420 × 420-pixel image of beta particle activity for four 9-mer probes that have hybridized with 21-mer target DNA. The exact matched site (C:G) appears much more active than the three mismatched sites. (b) Diagram showing sum of electron signal of all pixels within each quadrant.

7. ANALOG DEVICE TECHNOLOGY

7.1 CCD/CMOS FINITE-IMPULSE-RESPONSE FILTER

In a cellular phone or a TV receiver, a long (> 256-stage) finite-impulse-response (FIR) filter is required for channel equalization or ghost cancellation. A high-speed, low-power, charge-domain, bit-serial, pipelined multiplying digital-to-analog converter (MDAC) has been invented for this application. Based on this multiplier, an 18-stage digitally programmable FIR filter, shown in Figure 7-1, using a 1.2-μm double-polysilicon, double-metal CCD/CMOS process has been designed and is currently being fabricated by a MOSIS foundry.

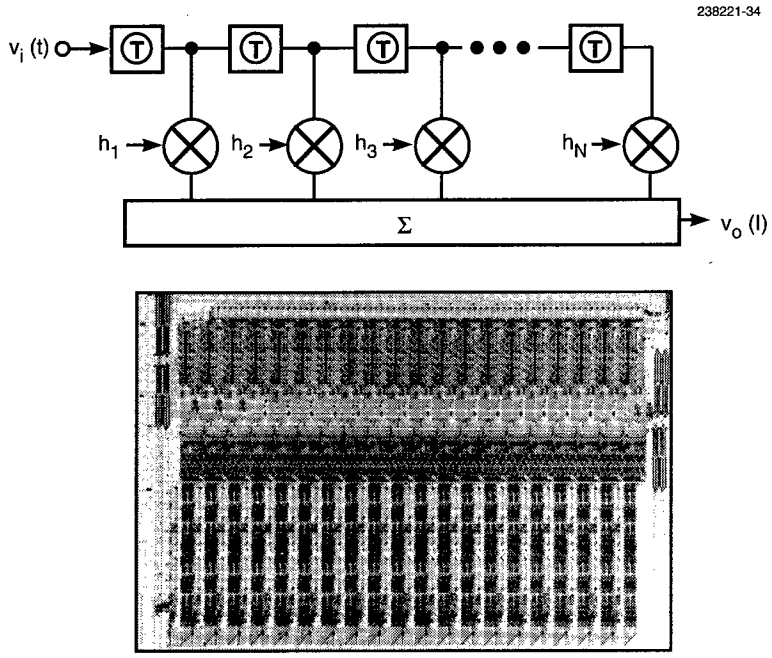

Figure 7-1. Block diagram and photograph of programmable CCD/CMOS finite-impulse-response filter.

A block diagram of the new MDAC is shown in Figure 7-2. The device computes the product of an analog quantity with an L-bit digital word, both in the signed-magnitude representation. In a direct-multiplication multiplier, let the multiplicand A be represented by a sign bit a_{sign} (0 for positive quantities, 1 for negative) plus its analog magnitude A^*, and let the multiplier B be an L-bit word given by

$$B = b_L + \sum_{i=1}^{L-1} b_{L-i} 2^{-i} = b_L + B^* \ , \tag{7.1}$$

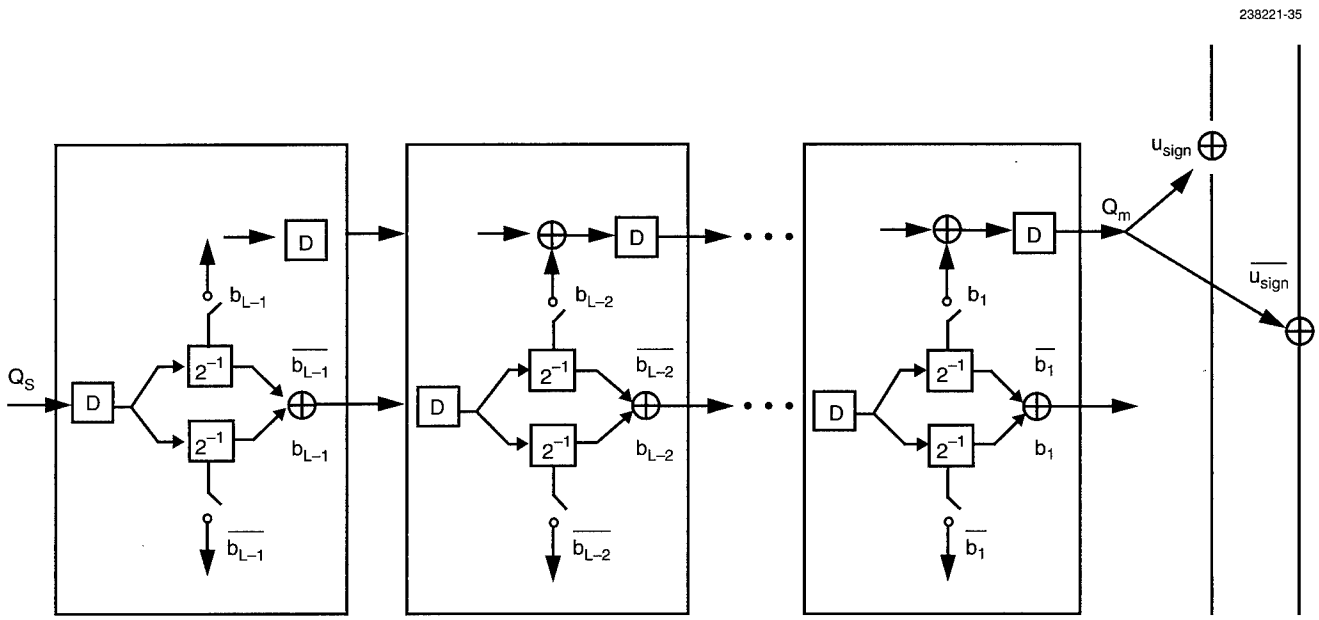

Figure 7-2. Charge-domain, pipelined, bit-serial multiplier.

where the b_i's are either 0 or 1 and, b_L is the sign bit defined as for a_{sign}. Let the product be the number U. We then have

$$U = AB = u_{\text{sign}} + A^*B^* = u_{\text{sign}} + A^*b_{L-1}2^{-1} + A^*b_{L-2}2^{-2} + \ldots + A^*b_1 2^{-(L-1)} \quad . \qquad (7.2)$$

Since the b_i's are 0 or 1, the binary multiplication is merely repeated additions, with the multiplicand properly shifted. The sign digit of the product u_{sign} is the XOR of the sign bits a_{sign} and b_L.

In a charge-domain implementation of the direct multiplication, the input multiplicand A is represented by a charge packet Q_s plus a sign bit, and if the input is accurate to 10 bits the charge packet will represent a 10-bit value. Test results demonstrate that better than 9-bit accuracy can be achieved in a divide-by-two charge-domain circuit with a 50-μm-long channel. To calculate the magnitude product of Q_sB^* as shown in Equation (7.2), only operations of dividing charge by two and adding charges are required. As shown in Figure 7-2, the device consists of L-1 processing stages, and each stage has a delay circuit, a divide-by-two charge-domain circuit, and an output summing-and-delay charge-domain buffer. Within each processing stage, the input charge Q_i is divided into two identical parts $Q_i/2$. The destination of one of the charge packets is controlled by the value of b_i, and the other half is always transferred to the next delay circuit. For example, if b_i =1, a charge packet equaling $Q_i/2$ will be transferred to the

output summing buffer located at the top of the multiplier, and the other charge packet will be transferred to the next processing stage. On the other hand, if $b_i = 0$, a charge packet equal to $Q_i/2$ will be discarded to an output drain and the other will be transferred to the next processing stage.

This divide-by-two-and-then-sum operation repeats for L–1 clock cycles. The amount of charge in the last stage of the output buffer will then equal

$$\sum_{i=1}^{L-1} Q_s 2^{-i} b_{L-i} \ , \tag{7.3}$$

which is the desired output representing the magnitude product of an analog quantity with a digital quantity. As can be seen from the above description, the device is implemented in a pipelined fashion, whereby a new input charge packet Q_s can be applied to the multiplier at every clock cycle. After an initial latency time of L–1 clocks, the device will have a continuous throughput rate equal to the input data rate. To compute the final four-quadrant output, the most-significant-bit of the digital word is XORed with the sign bit of the analog input. This generates a control signal for the sign bit u_{sign} of the final product. If it is 1, the charge packet will be transferred to the negative sum-of-the-product node; if 0, it will be transferred to the positive node.

A charge-domain, bit-serial, eight-stage, pipelined multiplier has been designed using 1.2-μm CCD/CMOS design rules provided by a MOSIS foundry. The chip area of this multiplier is 80 × 200 μm and the total capacitive load is 0.8 pF. The power required is only 600 μW for a 30-MHz, 5-V clock, or 22 pJ for each analog/digital multiplication. Based on this bit-serial multiplier, an 18-stage FIR has been designed in a 2-mm^2 chip area, as shown in Figure 7-1. This FIR filter offers a computation throughput rate of 25 000 MOPS/W. A comparison with FIR filter implementations using different technologies, shown in Table 7-1, clearly demonstrates the simultaneous speed and power advantages offered by the charge-domain computing technique.

A. M. Chiang

TABLE 7-1

Technology Comparison for Finite-Impulse-Response Filters

Technology	Performance (MOPS/W)	Functionality	Process	Accuracy
CCD MDAC	25,000	Multiply/add	2-Poly-Si, 2-metal 1.2 μm	Analog × 8 b
Digital CMOS [1]	2,300	Multiply/add	2-Poly-Si, 3-metal 1 μm	8 b × 8 b
HAC-3D [2]	130	Programmable	15-Layer wafer stack	Fixed-point
Alpha [3]	7	Microprocessor	2-Poly-Si, 3-metal 0.75 μm	64 b

REFERENCES

1. B. Edwards, A. Corny, N. Weste, and C. Greenberg, *Proceedings of Custom Integrated Circuits Conference* (IEEE, New York, 1992), p. 26.5.1.
2. C. Adams, *Mil. Aerosp. Electron.,* 26 (February 1991).
3. D. Dobberpuhl et al., *International Solid-State Circuits Conference Digest of Technical Papers* (IEEE, New York, 1992), p. 106.

REPORT DOCUMENTATION PAGE

Form Approved
OMB No. 0704-0188

1. AGENCY USE ONLY (*Leave blank*)	2. REPORT DATE	3. REPORT TYPE AND DATES COVERED
	~~15 February 1994~~	Quarterly Technical Report, 1 November 1993–31 January 1994

4. TITLE AND SUBTITLE

Solid State Research

5. FUNDING NUMBERS

C — F19628-90-C-0002
PE — 63250F
PR — 221

6. AUTHOR(S)

Alan L. McWhorter

7. PERFORMING ORGANIZATION NAME(S) AND ADDRESS(ES)

Lincoln Laboratory, MIT
P.O. Box 73
Lexington, MA 02173-9108

8. PERFORMING ORGANIZATION REPORT NUMBER

1994:1

9. SPONSORING/MONITORING AGENCY NAME(S) AND ADDRESS(ES)

HQ Air Force Materiel Command
AFMC/STSC
Wright-Patterson AFB, OH 45433-5001

10. SPONSORING/MONITORING AGENCY REPORT NUMBER

ESC-TR-94-085

11. SUPPLEMENTARY NOTES

None

12a. DISTRIBUTION/AVAILABILITY STATEMENT

Approved for public release; distribution is unlimited.

12b. DISTRIBUTION CODE

13. ABSTRACT (*Maximum 200 words*)

This report covers in detail the research work of the Solid State Division at Lincoln Laboratory for the period 1 November 1993 through 31 January 1994. The topics covered are Electrooptical Devices, Quantum Electronics, Materials Research, Submicrometer Technology, High Speed Electronics, Microelectronics, and Analog Device Technology. Funding is provided primarily by the Air Force, with additional support provided by the Army, ARPA, Navy, BMDO, and NASA.

14. SUBJECT TERMS

electrooptical devices, quantum electronics, materials research, submicrometer technology, high speed electronics, microelectronics, analog device technology, lasers, optical interconnects, microlens fabrication, ultraviolet lithography, optical-heterodyne generation, charge-coupled imagers, charge-coupled filters, genosensor technology

15. NUMBER OF PAGES 72

16. PRICE CODE

17. SECURITY CLASSIFICATION OF REPORT	18. SECURITY CLASSIFICATION OF THIS PAGE	19. SECURITY CLASSIFICATION OF ABSTRACT	20. LIMITATION OF ABSTRACT
Unclassified	Same as Report	Same as Report	Same as Report